Femtochemistry of Norrish Type-I Reactions: III. Highly Excited Ketones—Theoretical

Eric W.-G. Diau, Carsten Kötting, Theis I. Sølling, and Ahmed H. Zewail*[a]

*Time-dependant density functional theory (TDDFT) and ab initio methods (CASSCF and CASMP2) are applied here for the investigation of the excited-state potential energy surfaces of ketones studied experimentally in the accompanying paper, number IV in the series. The aim is to provide a general and detailed physical picture of the Norrish type-I reaction from S_0 and S_1 potentials (papers I and II) and from higher-energy potentials (papers III and IV). Particular focus here is on reactions following excitation to the 3s, 3p, and 3d Rydberg state and to the $(n_z \rightarrow \pi^*)$ and $(\pi \rightarrow \pi^*)$ valence states. It is shown that the active orbitals in the CASSCF calculations can be chosen so that accurate results are obtained with a small active space. Dynamic corrections of the state-specific CASSCF energies at the multireference MP2 level do not improve the results for the Rydberg states but are significant for the valence states. The geometries of the Rydberg states are similar to the ground state; the S_1 and other valence states are not. A common property of the valence states is the elongated CO bond and the pyramidalization of the carbonyl carbon atom. As a consequence, these valence states cross all Rydberg states along the CO stretching coordinate and provide an efficient pathway down to the 3s Rydberg states (S_2) through a series of conical intersections (**CI**s). The nonadiabatic coupling vector of the **CI** between the*

*$(\pi \rightarrow \pi^*)$ and the 3s Rydberg states guides energy channeling into the asymmetric CC-stretching mode. The energy demand for the CC bond breakage (Norrish type-I) on the S_2 surface is lower than that of the **CI** leading to the S_1 state. This CC bond breakage leads to a linear excited state acetyl radical (3s Rydberg). Crossing a small barrier the 3s acyl radical can access a **CI** leading either to a second CC bond breakage or to a hot ground-state acetyl radical. The barriers for the Norrish type-I reaction on the various excited-state surfaces can be rationalized within the framework of valence-bond theory. The dynamic picture of the Norrish type-I reactions is now clear: The excitation to high-energy states leads to the non-concerted breakage of the α-CC bonds by an "effective downhill" potential in space involving the active excitation center CO, CC stretching, and CCO bending nuclear motions, but not, as usually thought, a direct repulsive potential along the CC bond. In our accompanying paper (part IV), it is shown that the results from the experimental investigations of Norrish type-I reactions on the femtosecond timescale are consistent with these theoretical results.*

1. Introduction

The Norrish type-I (α-cleavage) reaction is an important and fundamental photochemical process of carbonyl compounds.[1] A classical example is the photodissociation of acetone, which has been the subject of numerous comprehensive investigations over many decades (see ref. [2] and references therein). The detailed α-cleavage reaction mechanism and the related dynamic behavior of this process are key to the understanding of the reactivity of the entire carbonyl family. In this laboratory, efforts have focused on real time studies of Norrish reactions— these studies focused on the issue of concertedness and on the time scale and mechanism for bond breakage.[2–4]

It is well established that the first singlet excited electronic state (S_1) of acetone is an $A_2(n_y \rightarrow \pi^*)$ valence state that is reached by the $\tilde{X}^1A_1 \rightarrow \tilde{A}^1A_2$ symmetry-forbidden transition (within the framework of C_{2v} symmetry). The S_1 transition gives rise to a weak and broad absorption band from 330 to 220 nm with its maximum around 280 nm (4.4 eV);[5] the intensity is "borrowed" from symmetry-allowed transitions through vibronic coupling. Early nanosecond fluorescence measurements[5, 6] indicate that the S_1 reaction kinetics of acetone is governed by

a rate-limiting $S_1 \rightarrow T_1$ intersystem crossing (ISC) process followed by α-cleavage on the T_1 surface. A recent study of the reaction dynamics using femtosecond-resolved mass spectrometry showed that for an excitation energy lower than the S_1 bond-breaking threshold, the ISC process is the rate-limiting step.[2] The α-cleavage process may proceed on the S_1 surface, as has been demonstrated for cyclobutanone, but an energy barrier must be surmounted.[2b, 7]

The second absorption band ($S_0 \rightarrow S_2$) in acetone results from a Rydberg-type transition giving the $B_2(n_y \rightarrow 3s)$ excited state. Energetically, both optical absorption[8, 9] and multiphoton ionization[10, 11] spectra of the 3s Rydberg state of acetone indicate that the 3s 0-0 band origin lies at 6.35 eV above its

[a] Prof. A. H. Zewail, Dr. E. W.-G. Diau, Dr. C. Kötting, Dr. T. I. Sølling
Arthur Amos Noyes Laboratory of Chemical Physics
California Institute of Technology
Pasadena, CA 91125, (USA)
Fax: (+ 1) 626-792-8456
http://www.its.caltech.edu/~femto/
E-mail: zewail@caltech.edu

ground-state minimum. Structurally, the two methyl torsion fundamentals (a_2 and b_1 modes) were observed to have frequencies much higher than the corresponding ground-state values,[8–10] suggesting that the equilibrium geometry of the ($n_y \rightarrow 3s$) state is significantly different from that of the ground state. However, as shown in this paper, the Rydberg and ground-state potentials are quite similar. The phenomenon of cluster-induced potential shifts, presumably brought about by both CO out-of-plane (b_1) and CCO in-plane (b_2) bending motions, were observed in the jet-cooled absorption spectrum in the S_2 region.[8b] These spectroscopic results lead the authors to propose a predissociation mechanism for the α-cleavage of acetone on the S_2 surface in which the reaction proceeds via a curve-crossing of the S_2 and the {S_1,T_1} manifold of states.

The photodissociation dynamics of acetone at 193 nm (6.4 eV) have been widely studied using various techniques.[12–16] For example, inferring from the dynamic information concerning the photofragment internal and translational energy distributions of the products, acetone in the S_2 state was proposed to dissociate exclusively into CO and two CH_3 radicals with the two CC bonds breaking in a stepwise manner.[16] This stepwise bond-breaking mechanism for the α-cleavage of acetone at 193 nm was found to be consistent with the observation of the significant rotational excitation of the product CO fragment.[12, 14] Recent femtosecond-resolved studies[17, 18] have shown that the S_2 lifetime (τ) of acetone at 195 nm (the 3s 0-0 band) is on the picosecond scale ($\tau \sim 3 - 5$ ps). Perdeuteration of acetone was found to increase the S_2 lifetime by a factor of two to three. To our knowledge, a detailed dynamic picture of the α-cleavage of acetone on the S_2 surface is still unavailable.

The available results regarding the spectroscopy, photochemistry, and reaction dynamics of acetone above the ($S_0 \rightarrow S_2$) transition are less informative than in the case of the S_1 and S_2 excited states. The most characterized electronic transitions of acetone beyond the S_2 state are the Rydberg-type excitations which involve the three distinct $n_y \rightarrow 3p$ transitions corresponding to the $A_2(n_y \rightarrow 3p_x)$, $A_1(n_y \rightarrow 3p_y)$, and $B_2(n_y \rightarrow 3p_z)$ states.[19, 20] The 0-0 transitions of the 3p Rydberg states were determined to lie above the ground state by 7.36, 7.41, and 7.45 eV for the A_2, A_1, and B_2 states, respectively.[19d] Although detailed analyses of the vibrational progressions of the 3p Rydberg spectra have been made,[19] direct dynamic information regarding the photophysical and photochemical processes is presently unavailable. The spectroscopic results indicate that the lowest-energy $A_2(n_y \rightarrow 3p_x)$ state has more pure Rydberg character than the others, whereas the $A_1(n_y \rightarrow 3p_y)$ state is significantly perturbed by the nearby $A_1(\pi \rightarrow \pi^*)$ valence state[20–22]—a general phenomenon which is known as Rydberg–valence interaction.[23] The substantial Rydberg–valence interaction between both A_1 states of acetone was argued to involve a nonadiabatic coupling via the CO stretching and/or the CO out-of-plane bending motions.[22] This coupling results in a reduction of the lifetime of the $A_1(n_y \rightarrow 3p_y)$ state by at least one order of magnitude compared to the B_2 or the A_2 3p Rydberg states. The properties of the $A_1(\pi \rightarrow \pi^*)$ valence state has yet to be observed experimentally. Therefore, the elucidation of the mechanism

for the Rydberg–valence interactions between the $A_1(n_y \rightarrow 3p_y)$ and the $A_1(\pi \rightarrow \pi^*)$ states of acetone will have to rely on theoretical investigations.

Quantum chemical calculations[24–28] using various sophisticated ab initio methods have mainly focused on reproducing the experimental vertical-excitation spectrum of acetone. The subject of Rydberg–valence interactions for the A_1 3p and 3d states of acetone was addressed computationally using for the first time the CASPT2 approach. The potential energy surface (PES) of the $A_1(\pi \rightarrow \pi^*)$ state was found to cross with the other two A_1 Rydberg states along the CO bond-stretching coordinate under the restriction of C_{2v} symmetry.[28] However, the interaction between the Rydberg and the valence excited states, which was assumed to be weak and therefore ignored in the calculations, was later found to be significant. This is supported by the results for the Rydberg spectrum of acetone, which shows substantial $A_1(\pi \rightarrow \pi^*)$ valence character in the $A_1(n_y \rightarrow 3p_y)$ Rydberg state.[22] Note that in the case of formaldehyde, it has been shown that the Rydberg states are considerably affected by the valence interaction with the ($\pi \rightarrow \pi^*$) state over almost the entire span of Rydberg states.[23]

The absorption spectrum of acetone above the 3p Rydberg region is more complex. Recent experimental investigations using the jet-cooled (3+1) resonance-enhanced multiphoton ionization (REMPI) technique, in combination with ab initio calculations, have assigned the three absorption bands around 8 eV to be the $A_1(n_y \rightarrow 3d_{yz})$, $B_2(n_y \rightarrow 3d_{x^2-y^2})$, and $B_1(n_y \rightarrow 3d_{xy})$ Rydberg states. The structured feature around 7.8 eV together with underlying near-continuum background show that the $A_1(n_y \rightarrow 3d_{yz})$ Rydberg state in that absorption region is strongly perturbed by the $A_1(\pi - \pi^*)$ valence state and/or the presence of a repulsive potential. Similar to the example of the Rydberg–valence interaction between the Rydberg ($n_y \rightarrow 3p_y$) and the valence ($\pi \rightarrow \pi^*$) states, the outcome of such a Rydberg–valence interaction with the $A_1(n_y \rightarrow 3d_{yz})$ state gives rise to the diffuse absorption feature with a very short lifetime for the 3d Rydberg state. In fact, recent femtosecond studies in this excitation-energy region (~ 8 eV) have shown that the lifetime of the 3d Rydberg states is as short as 50 fs when a two-photon excitation is applied[3a] or 330 fs with excitation by a single photon.[29]

As pointed out in recent theoretical work, the spectra of higher-lying states of ketones are significantly influenced by the Rydberg–valence state mixing and that dissociation is not expected to be direct.[23] Since the mechanism for the Norrish type-I reaction of acetone taking place on the $S_1(n,\pi^*)$ surface has been given elsewhere,[2] the goal of the present study is to provide a general dynamic picture for α-cleavage of ketones occurring beyond the $S_1(n,\pi^*)$ state. The present work is a continuation of our previous studies[2] of the femtochemistry of Norrish type-I reactions of ketones with focus on the characterization of the potential energy surfaces of acetone using multiconfiguration (MC) self-consistent field (SCF) and time-dependent (TD) density functional theory (DFT) methods.[30, 31] The accompanying paper gives the experimental results for 13 ketones and the comparisons with the theoretical findings reported here.

Computational Methods

The strategy for the CASSCF calculations is to find a proper active space which is capable of describing the excited-state PESs for acetone. The 6-311+G(d,p) basis set is used in most of the calculations. The orbitals were first optimized at the Hartree – Fock level and then appropriately selected into the active space for the subsequent CASSCF calculations. The choice of the orbitals in the active space depends on the type of the excited states to be studied. For example, two sets of CC σ and σ^* orbitals, one set of CO π and π^* orbitals, and two nonbonding orbitals are good choices for the active space to describe the ground-state and the first excited-state PES.[2] For describing the high-energy excited-state PESs with Rydberg characters, different type of the Rydberg molecular orbitals (MOs) must be included in the active space. Figure 1 shows the relevant MOs which have been employed in our CASSCF calculations.

For most of the surface-scan calculations, the geometry of each species along the scanning coordinate (either CO or α-CC bond distance) was first optimized on the ground-state surface (either for the neutral or cationic species) using the B3LYP functional combined with the 6-31+G(d) basis set. Then the single-point energy calculations were carried out using either the TDDFT approach at the TD-B3LYP/6-31+G(d) level of theory, or the state-average (sa-) CASSCF approach at the CAS(6,7)/6-311+G(d,p) level of theory. Furthermore, the vertical excitation energies of acetone were also calculated at the TD-B3P86/6-311++G(d,p) and the CAS(8,16)/6-311+G(d,p) levels of theory. The CAS(8,16) calculations were performed using MOLPRO 2000.[51] The remaining TDDFT and CASSCF calculations were carried out using the Gaussian 98 package.[46]

2. Results and Discussion

2.1. Vertical Excitation Spectrum of Acetone

The theoretical predictions of the vertical excitation spectrum of acetone have been reported based on configuration – interaction (CI),[24] the random-phase approximation,[25] equation-of-motion coupled-clusters,[26] CASSCF(6,14),[27] CASPT2,[28] and TDDFT[30] approaches. A good agreement between theory and

experiment has been found.[28] Our goal here is to understand the limit of the computations employed presently and to find the best strategy for further exploration of the global excited-state PESs. Three different computational approaches were used—TDDFT, and state-averaged and state-specific CASSCF (ss- and sa-CASSCF) methods. Table 1 shows the comparison between the calculated results at various levels and those obtained from experiments.

2.1.1. Time-Dependent DFT Calculations

The TDDFT approach has been recognized to be an inexpensive and reasonably accurate method for determination of the vertical excitation energies.[31] In a recent theoretical work,[30] a series of hybrid density functionals were tested for the excitation energies of acetone. It was found that the B3P86 functional in combination with the 6-311++G(d,p) basis set give the best agreement with the experimental values. Therefore we employed for acetone in a previous study the B3P86/6-311++ G(d,p) level to calculate the vertical excitation energies and the corresponding oscillator strengths of an extended series of excited states.[2] Two sets of TDDFT results are summarized in Table 1. It is worth noting that the results obtained at the cost-effective TD-B3LYP/6-31+G(d) level are similar to those obtained at the TD-B3P86/6-311++G(d,p) level. Thus, the elaborated surface-scan calculations in the present study were carried out at the TD-B3LYP/6-31+G(d) level.

2.1.2. State-Averaged CASSCF Calculations

Our first computational attempt to reproduce the experimental excitation spectrum of acetone is to perform an sa-CASSCF calculation using an active space which is so large that the excitations for most of the Rydberg and valence excited states are predicted accurately. This was done in two state-averaged calculations, each with eight electrons in sixteen orbitals.[32] The MOs in the two active spaces are shown in Figure 1. Table 1

Electronic state	TD-B3LYP /6-31+G(d)	TD-B3P86 /6-311++G(d,p)	sa-CAS(8,16) /6-311+G(d,p)	sa-CAS(8,8) /6-311+G(d,p)	sa-CAS(6,7) /6-311+G(d,p)	sa-CAS(6,8) /6-311+G(d,p)	CAS/MP2[b] /6-311+G(d,p)	CASPT2[c]	Expt.[d]
$A_2(n_y \rightarrow \pi^*)$	4.40	4.40	4.76	4.48	4.75	4.53	4.57/4.04	4.18	4.38
$B_2(n_y \rightarrow 3s)$	6.17	6.25	5.97	6.19	6.16	6.47	6.35/[e]	6.58	6.35
$A_1(n_y \rightarrow 3p_y)$	7.07	7.19	7.18	7.52	7.38	7.68	7.32/[e]	7.26	7.41
$A_2(n_y \rightarrow 3p_x)$	7.37	7.42	7.07					7.34	7.36
$B_2(n_y \rightarrow 3p_z)$	7.42	7.64	7.08					7.48	7.45
$B_2(n_y \rightarrow 3d_{x^2-y^2})$	7.71	7.87	7.80					8.04	8.09
$A_1(n_y \rightarrow 3d_{yz})$	8.08	8.07	8.19					7.91	7.80
$B_1(n_y \rightarrow 3d_{xy})$	8.33	8.33	8.11					8.20	8.17
$B_2(n_y \rightarrow 3d_{z^2})$	8.54	8.51	8.17		8.20			8.18	
$A_2(n_y \rightarrow 3d_{xz})$	8.87	8.98	8.49					8.09	
$A_1(\pi \rightarrow \pi^*)$	8.84	8.87	9.95	11.04		10.87	10.67/8.83	9.16	
$B_1(n_z \rightarrow \pi^*)$	8.67	8.70			10.38	10.08	10.03/8.89	9.10	
$A_2(\sigma' \rightarrow \pi^*)$	8.36	8.30	10.49	10.45					
$B_1(\pi \rightarrow 3s)$	8.88	8.99	9.32	9.32	8.98	9.19			
$A_2(\pi \rightarrow 3p_y)$	9.71	9.88	10.40	10.58	10.16	10.40			

Table 1. *Calculated excitation energies for acetone.[a]*

[a] All calculations are based on singlet states, values in eV; the *x*, *y*, and *z* axes are defined in Figure 4. [b] The values before and after the slash correspond to the state-specific CASSCF and the corresponding CASMP2 results, respectively; see text for the details regarding the active space. [c] From ref. [28]. [d] From refs. [19, 28]. [e] The deviations from experimental results are not uniform, see Table 2.
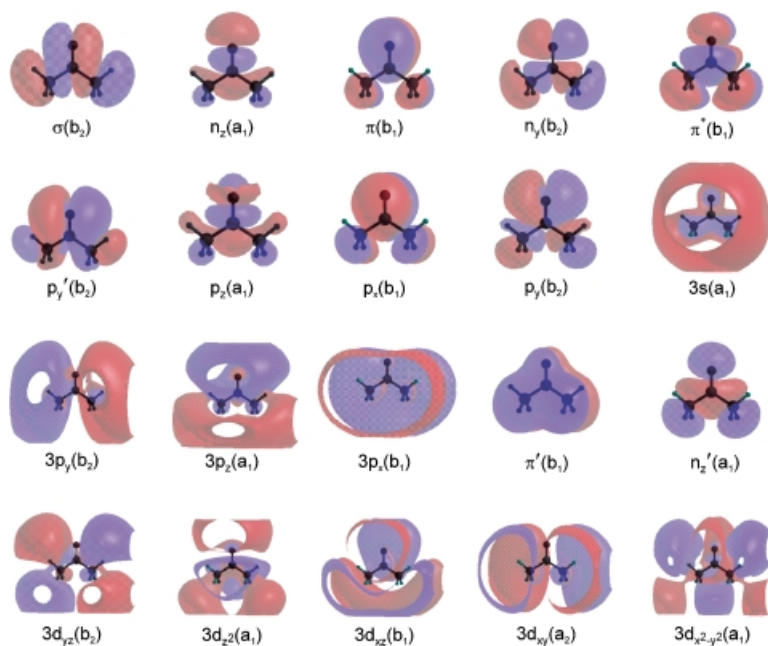
Figure 1. *Molecular orbitals (MOs) of acetone. The active space orbitals of the various CASSCF calculations in the present study where chosen among these MOs (for details regarding the particular calculations, see text).*

summarizes the results. The maximum deviation from experiment is ± 0.4 eV. The excitation energy of the $S_1(n,\pi^*)$ state was overestimated by ~ 0.4 eV and that of the $S_2(n,3s)$ state was underestimated by ~ 0.4 eV. A series of test calculations shows that a smaller deviation can be obtained by using a smaller active space. For example, in an sa-CAS(8,8)/6-311+G(d,p) calculation, where the original twelve ground-state virtual orbitals in the CAS(8,16) calculations are now reduced to four MOs ($\pi^*(b_1)$, $3s(a_1)$, $3p_y(b_2)$, and $p_z(a_1)$), the energy of the S_1 state relative to the ground state was overestimated by only 0.1 eV and the relative energy of the S_2 state was underestimated by 0.15 eV. This sa-CAS(8,8) calculation also successfully predicts the excitation energies to the $A_2(n_y \rightarrow \pi^*)$, the $B_2(n_y \rightarrow 3s)$, and the $A_1(n_y \rightarrow 3p_y)$ states with an accuracy of ± 0.1 eV. However, all excitation energies relating to the higher-energy valence excited states, such as the $A_1(\pi \rightarrow \pi^*)$ and the $B_1(n_z \rightarrow \pi^*)$ states, still are substantially overestimated at the sa-CASSCF levels in comparison with those predicted at higher levels (Table 1). Therefore, additional dynamic electron correlation may be needed to accurately predict the excitation energies for the valence states beyond the first excited singlet state ($S_1(n,\pi^*)$). This refinement of the electron-correlation description will be introduced in the following Section.

2.1.3. State-Specific CASSCF and CASMP2 Calculations: The $B_2(n_y \rightarrow 3s)$ Rydberg State

The sa-CASSCF method includes some electron correlation through orbital relaxation.[33] The effect of dynamic correlation can be described using the multireference (MR) Møller–Plesset perturbation theory to the second-order (MP2).[34, 35] The present study aims at the characterization of the high-energy excited

PESs of acetone beyond the S_1 state. Five excited states—two Rydberg states and three valence states (see below)—are investigated using the ss-CASSCF method. Furthermore, the dynamic correlation of each valence state has been included through the MR calculations at the ss-CASSCF/MP2 (CASMP2) level. The excellent agreement between the CASMP2 predictions presented herein, the CASPT2, and the experimental results for the vertical excitation energies of acetone (Table 1) ensures that the MOs in our CASSCF calculations were appropriately chosen; details will be given in the following.

The lowest-lying Rydberg excited state of acetone is due to the $n_y \rightarrow 3s$ transition. This corresponds to the lowest-lying symmetry-allowed singlet–singlet absorption and the second lowest transition between two singlet states ($S_0 \rightarrow S_2$). In order to properly describe the vertical excitation to the $B_2(n_y \rightarrow 3s)$ Rydberg state in an efficient manner, the following strategy was employed: Generally, the smallest-sized active space that reasonably describes the excitation in question is employed in the ss-CASSCF calculations. Specifically for the $B_2(n_y \rightarrow 3s)$ state, the $\pi^*(b_1)$ orbital (Figure 1) is left out of the active space so that the $n_y \rightarrow 3s$ transition becomes the second root of the CI equations. The above computational procedure is very successful in characterizing the adiabatic excited-state PESs of acetone not only for the $B_2(n_y \rightarrow 3s)$ Rydberg state but also for the other Rydberg and valence states under study.

We have investigated the stability and the accuracy of the present ss-CASSCF approach using only a very limited number of orbitals as the active space. The results for the vertical excitation energy of the $B_2(n_y \rightarrow 3s)$ Rydberg state of acetone are summarized in Table 2 for nine different active spaces, which include one CAS(4,4), one CAS(6,4), two different CAS(6,5), two different CAS(6,6), one CAS(6,7), and two different CAS(8,7) calculations. For example, the four active orbitals in the CAS(4,4) calculation are the two ground-state occupied orbitals, $\pi(b_1)$ and $n_y(b_2)$, and the two ground-state virtual orbitals, $3s(a_1)$ and $p_y(b_2)$; in the CAS(6,4) calculations we have chosen the three occupied orbitals to be the $\sigma(b_2)$, $\pi(b_1)$, and $n_y(b_2)$ MOs, and the only virtual orbital to be the $3s(a_1)$ MO; the active spaces in the other ss-CASSCF calculations were chosen similarly (Table 2).

All the solutions corresponding to the second roots of the CI equations in nine ss-CASSCF calculations have only one dominant electronic configuration corresponding to the $n_y \rightarrow 3s$ transition (B_2; the corresponding CI coefficient is greater than 0.98). To correctly predict the vertical excitation energy of the $B_2(n_y \rightarrow 3s)$ Rydberg state, the orbitals corresponding to the second-root solution were used as a starting guess in the calculation of the ground-state energy (the first root of the CI equations). The excitation energy is given by $\Delta E = E(S_2) - E(S_0)$. This procedure assures that the search for the first and the second root of the CI equations involves the same set of orbitals in the active space. Even though different active electrons and orbitals were used in all of the nine calculations (Table 2), the predicted ΔE values are indeed in good agreement (within at

Table 2. Total energies for the $B_2(n_y, 3s)$ state and the energy relative to the ground state (ΔE) calculated at the CASSCF/6-311 + G(d,p) and CASMP2/6-311 + G(d,p) levels.

m,n[a]	Active orbitals[b]	E(CASSCF)[c]	ΔE[d]	E(CASMP2)[c]	ΔE[d]
4,4	$\pi(b_1)$, $n_y(b_2)$, $3s(a_1)$, $p_y(b_2)$	− 191.78954	6.46	− 192.48586	6.42
6,4	$\pi(b_1)$, $\sigma(b_2)$, $n_y(b_2)$, $3s(a_1)$	− 191.78945	6.14	− 192.45498	7.50
6,5	$\pi(b_1)$, $\sigma(b_2)$, $n_y(b_2)$, $3s(a_1)$, $p_y(b_2)$	− 191.79913	6.20	− 192.50707	5.81
6,5	$\pi(b_1)$, $\sigma(b_2)$, $n_y(b_2)$, $3s(a_1)$, $p_x(b_1)$	− 191.81952	6.21	− 192.45143	7.79
6,6	$\pi(b_1)$, $\sigma(b_2)$, $n_y(b_2)$, $3s(a_1)$, $p_y(b_2)$, $p'_y(b_2)$	− 191.80282	6.30	− 192.50180	6.77
6,6	$\pi(b_1)$, $\sigma(b_2)$, $n_y(b_2)$, $3s(a_1)$, $p_x(b_1)$, $p_y(b_2)$	− 191.83475	6.54	− 192.50299	6.29
6,7	$\pi(b_1)$, $\sigma(b_2)$, $n_y(b_2)$, $3s(a_1)$, $p_z(a_1)$, $p_x(b_1)$, $p_y(b_2)$	− 191.83747	6.58	− 192.49112	7.29
8,7	$n_z(a_1)$, $\pi(b_1)$, $\sigma(b_2)$, $n_y(b_2)$, $3s(a_1)$, $p_x(b_1)$, $p_y(b_2)$	− 191.83720	6.47	− 192.56808	4.56
8,7	$n_z(a_1)$, $\pi(b_1)$, $\sigma(b_2)$, $n_y(b_2)$, $3s(a_1)$, $p_z(a_1)$, $p_y(b_2)$	− 191.82624	6.32	− 192.48890	6.62

[a] m,n is the number of active electrons and active orbitals, respectively. [b] See Figure 1. [c] Values in hartree. [d] Values in eV.

least 0.4 eV) regardless whether the active space is medium sized (for example, CAS(6,7) with a total of 470 configuration state functions (CSFs)) or small (for example, CAS(6,4) with a total of only 10 CSFs). Interestingly, the mean of the nine ss-CASSCF ΔE values is 6.35 eV, which is in excellent agreement with the experimental result (6.35 eV; Table 1).

The CASMP2 calculations on the vertical excitation energy of the $B_2(n_y \rightarrow 3s)$ Rydberg state have been performed using the same CASSCF wavefunctions after convergence to the first root for the S_0 state or the second root for the S_2 state. The results are also shown in Table 2 with the surprising result that the ΔE values of the 3s Rydberg state predicted at the CASMP2 levels are scattered in the wide range of 4.6 – 7.8 eV! In the early CASPT2 calculations based on a larger active space with more basis functions,[28] it was found that the vertical excitation energy of the 3s Rydberg state predicted at the CASSCF level is somewhat lower than that predicted at the CASPT2 level (6.39 eV at the CASSCF level versus 6.58 eV at the CASPT2 level).[28] Similar results were also obtained using our approach at the CAS(6,6) level (6.30 versus 6.77 eV) and the CAS(8,7) level (6.32 versus 6.62 eV; Table 2). Both results show the negative effect for the dynamic electron correlation at the CASMP2 level, namely, more correlation was made for the ground state than for the 3s Rydberg state. However, positive dynamic correlation has been found in our other CASMP2 calculations (Table 2), indicating that the CASMP2 calculations for the Rydberg states based on the present approach are not reliable. As a consequence, our benchmark investigation for evaluation of the vertical excitation energy to the 3s Rydberg state (Table 2) suggests that the relatively cost-effective ss-CASSCF approach is preferable to the more time-consuming CASMP2 method in the characterization of the PES for this and other Rydberg states.

2.1.4. State-Specific CASSCF and CASMP2 Calculations: The $A_1(n_y \rightarrow 3p_y)$ Rydberg State

The aforementioned ss-CASSCF procedure for the $B_2(n_y \rightarrow 3s)$ Rydberg state was also employed to calculate the vertical excitation energy for the $A_1(n_y \rightarrow 3p_y)$ Rydberg state. For example, in the CAS(6,4) calculations, the three ground-state

occupied orbitals are the $\sigma(b_2)$, $\pi(b_1)$, and $n_y(b_2)$ MOs, and the only necessary virtual orbital is now the $3p_y(b_2)$ MO as shown in Figure 1. However, when solving for the second root, two of the resulting orbitals have changed significantly to become Rydberg/lone-pair mixtures (($n_y - 3p_y$) and ($n_y + 3p_y$), Figure 2). The
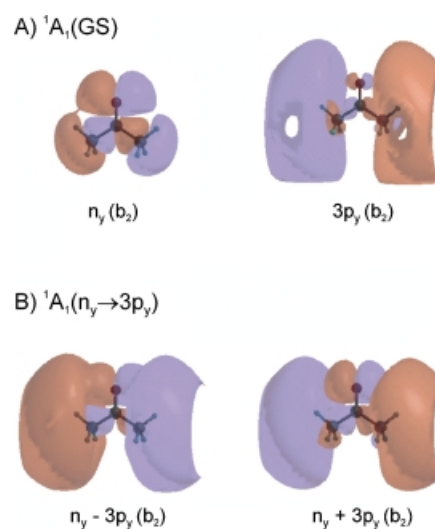

Figure 2. A) Orbitals calculated at the state-specific CAS(6,4)/6-311 + G(d,p) level when solving for the first root. B) The corresponding orbitals that result when the second root ($A_1(n_y \rightarrow 3p_y)$) is sought. It seems that the set in B) can be described as a linear combination of the set in A).

second root of the CI equations does not correspond to a pure transition (the $3p_y$ Rydberg state) as in the case of the $B_2(n_y \rightarrow 3s)$ Rydberg state. Instead, it is a mixture of two electronic configurations. Interestingly, in each of the two configurations, one of the Rydberg/lone-pair hybrid orbitals (either ($n_y - 3p_y$) or ($n_y + 3p_y$)) is doubly occupied whereas the other one is empty. This finding indicates that the Rydberg – valence interaction is described at the MO level;[23] in Section 2.3.2 we show that when the computation involves a larger active space the Rydberg – valence interaction is described primarily at the CI level. The ΔE value was determined to be 7.32 eV, which is in excellent agreement with the experimental value ($\Delta E_{exp} = 7.41$ eV; Table 1).

2.1.5. State-Specific CASSCF and CASMP2 Calculations: The A₂(n_y →π*) Valence State

The first singlet excited state (S_1) of acetone arises from the symmetry-forbidden ($n_y \rightarrow \pi^*$) transition ($^1A_2$). The associated PES has been thoroughly characterized in the first two papers of this series.[2] The vertical excitation energy to reach the $A_2(n_y \rightarrow \pi^*)$ valence state is well established. The goal of this Section is to verify that the ΔE value calculated by the present ss-CASSCF/MP2 approach is reasonable before it is employed to further characterize the PES for other valence excited states.

We started from a simple CAS(4,4) approach, where the active space is chosen to consist of two ground-state occupied orbitals ($\pi(b_1)$ and $n_y(b_2)$) and two virtual orbitals optimized for the ground state ($\pi^*(b_1)$ and $p_y(b_2)$; Figure 1). The second root of the CI equations at this CAS(4,4) level corresponds to the desired $n_y \rightarrow \pi^*$ transition with the corresponding CI coefficient equal to 0.999. The results for ΔE are given in Table 3. At the CAS(4,4) level, the ΔE values of the $A_2(n_y \rightarrow \pi^*)$ state are overestimated by ~ 0.7 eV, and further MRMP2 corrections do not recover the dynamic correlation energy of the valence state to a meaningful extent. However, the ΔE values of the $A_2(n_y \rightarrow \pi^*)$ state are reduced to 4.8 eV with one additional occupied orbital, $\sigma(b_2)$, being added into the active space. The CASMP2 calculations based on the CAS(6,5) wavefunctions improved the result; a reduction in ΔE of 0.35 eV (to 4.45 eV) was found using the 6-311 + G(d,p) basis set. Note that the experimental ΔE value of the $A_2(n_y \rightarrow \pi^*)$ state is 4.38 eV (Table 1). The excellent agreement for the vertical excitation energy of the $A_2(n_y \rightarrow \pi^*)$ valence state between the CASMP2 approach and experiment shows that such a simple theoretical model can be used with confidence to further characterize other high-energy valence excited states where the experimental results are not yet available.

2.1.6. State-Specific CASSCF and CASMP2 Calculations: The A₁(π →π*) Valence State

Because of the successful description of the $A_2(n_y \rightarrow \pi^*)$ valence state, a similar strategy has been applied to characterize the PES of the $A_1(\pi \rightarrow \pi^*)$ valence state. Only two pairs of MOs, the π_{CO}/π_{CO}^* (represented by $\pi(b_1)$ and $\pi^*(b_1)$ in Figure 1) and the $\sigma_{CO}/\sigma_{CO}^*$ (represented by $n_z(a_1)$ and $p_z(a_1)$ in Figure 1), were included in a CAS(4,4) calculation. The MOs that result when solving for the first and the second root are shown in Figures 3A and 3B, respectively. The MOs calculated at the CAS(6,5) level with one
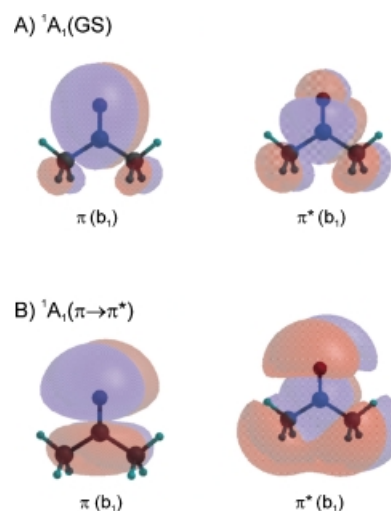

Figure 3. A) Orbitals calculated at the state-specific CAS(4,4)/6-311 + G(d,p) level when solving for the first root. B) The corresponding orbitals when the second root ($A_1(\pi \rightarrow \pi^*)$) is sought. It seems that the set in B) can be described as a distorted version of the set in A).

additional occupied orbital ($\pi'(b_1)$) in the active space are similar. In the case of the CAS(4,4) calculation, the second root of the CI equations involves two major electronic configurations. Interestingly, the ground-state (first root) $\pi(b_1)$ and $\pi^*(b_1)$ orbitals become substantially "distorted" in the case of the second root. This feature is analogous to the result for the $A_1(n_y \rightarrow 3p_y)$ Rydberg state and is an indication that the Rydberg–valence interaction is most appropriately described at the MO level for this particular active space.

The ΔE value at the CAS(4,4) level was determined to be 10.70 eV using the 6-311 + G(d,p) basis set. The CASMP2 corrections have significantly reduced the ΔE value to 9.90 eV. Further improvement of the ΔE value may be achieved by the expansion of the active space of the CAS(4,4) calculation. In the present study, we have found a dramatic effect in recovering the dynamic correlation energy for the $A_1(\pi \rightarrow \pi^*)$ valence state of acetone through a CASMP2 calculation using the CAS(6,5) wavefunction with one additional occupied orbital, $\pi'(b_1)$, being added into the original (CAS(4,4)) active space (Table 3). In particular, the ΔE value was determined to be 8.83 eV at the ss-CASMP2/6-311 + G(d,p) level of theory, which is slightly lower than the recent CASPT2 result (9.16 eV; Table 1) but in perfect agreement with our results calculated using the TDDFT approach (8.84 and 8.87 eV; Table 1).

Table 3. Total energies for the $A_1(\pi \rightarrow \pi^*)$, $B_2(n_z \rightarrow \pi^*)$, and $A_2(n_y \rightarrow \pi^*)$ states and the energy relative to the ground state (ΔE) calculated at the CASSCF/6-311 + G(d,p) and CASMP2/6-311 + G(d,p) levels.

Electronic state	m,n[a]	Active orbitals[b]	E(CASSCF)[c]	ΔE[d]	E(CASMP2)[c]	ΔE[d]
$A_2(n_y \rightarrow \pi^*)$	4,4	$\pi(b_1)$, $n_y(b_2)$, $\pi^*(b_1)$, $p_y(b_2)$	− 191.88535	5.15	− 192.53531	5.24
$A_2(n_y \rightarrow \pi^*)$	6,5	$\pi(b_1)$, $\sigma(b_2)$, $n_y(b_2)$, $\pi^*(b_1)$, $p_y(b_2)$	− 191.89823	4.80	− 192.56642	4.45
$B_1(n_z \rightarrow \pi^*)$	6,5	$n_z(a_1)$, $n_z'(a_1)$, $\pi(b_1)$, $\pi^*(b_1)$, $p_z(a_1)$	− 191.72027	10.03	− 192.39926	8.89
$A_1(\pi \rightarrow \pi^*)$	4,4	$n_z(a_1)$, $\pi(b_1)$, $\pi^*(b_1)$, $p_z(a_1)$	− 191.69313	10.70	− 192.35450	9.90
$A_1(\pi \rightarrow \pi^*)$	6,5	$n_z(a_1)$, $\pi(b_1)$, $\pi'(b_1)$, $\pi^*(b_1)$, $p_z(a_1)$	− 191.69434	10.67	− 192.35028	8.83

[a] m,n is the number of active electrons and active orbitals, respectively. [b] See Figure 1. [c] Values in hartree. [d] Values in eV.

2.1.7. State-Specific CASSCF and CASMP2 Calculations: The $B_1(n_z \rightarrow \pi^*)$ Valence State

The strategy for the $B_1(n_z \rightarrow \pi^*)$ valence state is very similar to that for the $A_1(\pi \rightarrow \pi^*)$ valence state, namely forcing the desired $(n_z \rightarrow \pi^*)$ transition (B_1) to be the second root of the CI equations. Because the vertical excitation energies of both the $B_1(n_z \rightarrow \pi^*)$ and the $A_1(\pi \rightarrow \pi^*)$ states are very close (Table 1), a slight change in the small active space may consequently alter the order of the two states in the CI solutions based on present CASSCF approach. Our investigations indicate that the originally active $\pi'(b_1)$ orbital in the CAS(6,5) calculations for the $A_1(\pi \rightarrow \pi^*)$ state needs to be replaced by the $n'_z(a_1)$ orbital in order for the $B_1(n_z \rightarrow \pi^*)$ state to become the second root of the CI equations in the same calculations. Note that the CI coefficient corresponding to the $(n_z \rightarrow \pi^*)$ transition (B_1) was determined to be 0.988 in the CAS(6,5) calculation.

The results of the vertical excitation energy of the $B_1(n_z \rightarrow \pi^*)$ state are shown in Table 3. The significance of the dynamic correlation for the valence excited states is again demonstrated. The ΔE value of the $B_1(n_z \rightarrow \pi^*)$ state has been predicted to be 10.03 eV at the CAS(6,5)/6-311 + G(d,p) level of theory and is dramatically reduced to 8.89 eV in the subsequent CASMP2 calculation.

2.2. Characterization of the Excited-State Geometries

The present ss-CASSCF description of the vertical spectrum for the five excited states of acetone investigated seems to be successful. We therefore take the next step and investigate the key features of the PESs for these five excited states. The PES of the first excited state of acetone has been well characterized.[2] In the following we focus on the calculation of the symmetry-constrained geometries of the other four excited states.

2.2.1. The $B_2(n_y \rightarrow 3s)$ Rydberg State

The structural features on the 3s Rydberg state are investigated at the CAS(6,6)/6-311 + G(d,p) level of theory with the symmetry constrained to C_{2v}; the result is shown in Figure 4A. The close resemblance to the ground-state species is evident, only the CO bond distance (r(CO) = 1.19 Å) is shorter by 0.04 Å compared to the ground state. The frequency calculation gives one imaginary value (104i cm^{-1}) which corresponds to the asymmetric torsional motion of the methyl groups (a_2 mode); the normal-coordinate vector is shown in Figure 4A. This mode lowers the symmetry from C_{2v} to C_2. By carefully choosing the appropriate MOs in the active space and by distortion of the symmetry to C_2, the optimized geometry of the 3s Rydberg state was obtained with
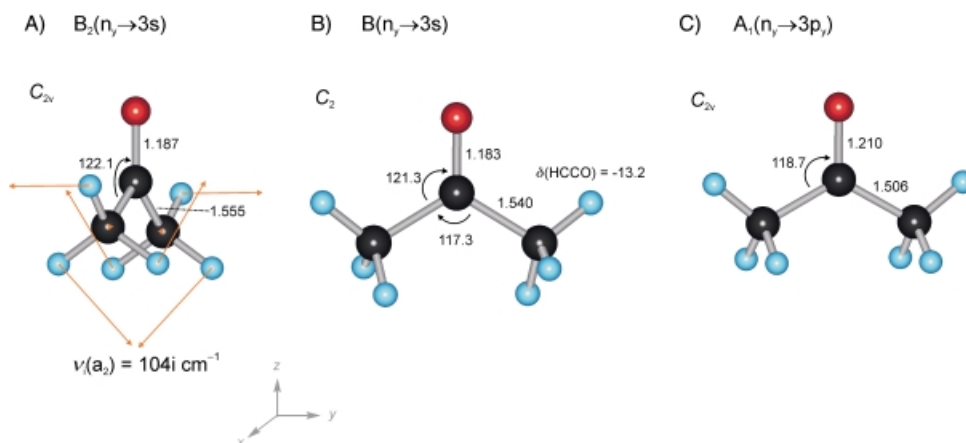

Figure 4. The structures and relevant geometrical parameters of A) the $B_2(n_y \rightarrow 3s)$, B) the $B(n_y \rightarrow 3s)$, and C) the $A_1(n_y \rightarrow 3p_y)$ species optimized at the CAS(6,6)/6-311 + G(d,p) level. The normal-coordinate vector shown in A) represents the nuclear motion (the a_2-symmetric CH$_3$ torsion) corresponding to the imaginary frequency of this species.

no imaginary frequencies at the CAS(6,6) level (Figure 4B). Note that structures which are almost identical to that shown in Figure 4B were obtained at both the CAS(8,7)/6-311 + G(d,p) and the CAS(6,7)/6-311 + G(d,p) levels of theory.

Table 4 lists the calculated vibrational frequencies of the $(n_y \rightarrow 3s)$ Rydberg state of acetone and its hexadeuterated isotopomer with both C_{2v} and C_2 symmetries. We also include the experimental values of six active vibrational modes of the excitation to the 3s Rydberg state (in the parentheses of Table 4) for comparison. Three points need to be mentioned: First, the vibrational frequencies corresponding to the three CH$_3$ deformating a_1 modes (ν_4, ν_5, and ν_6) were somewhat overestimated by theory whereas the other three low-frequency modes (ν_8, ν_{12}, and ν_{17}) are in good agreement with theory.[8a, 10] Second, the ratios between the calculated vibrational frequencies for [D$_0$]- and [D$_6$]acetone are indeed in excellent accordance with experiment.[19d] This agreement provides theoretical support for the early experimental observations and for the subsequent spectral analyses and assignments to be correct. Third, our ab initio calculations have confirmed that excitation to the 3s Rydberg state causes the methyl groups of the excited-state acetone to counter-rotate by ~ 15° from the eclipsed – eclipsed C_{2v} ground-state equilibrium geometry. The calculated frequencies for the C_{2v} and the C_2 species are almost identical (Table 4) except for the two torsional modes, $\nu_{12}(a_2)$ and $\nu_{17}(b_1)$. Note that the question of whether the equilibrium structure of acetone in the 3s Rydberg state has either C_{2v} or C_2 symmetry has been addressed experimentally but an answer was not found.[10]

2.2.2. The $A_1(n_y \rightarrow 3p_y)$ Rydberg State

The geometry of the 3p$_y$ Rydberg state has been optimized at the CAS(6,6)/6-311 + G(d,p) level of theory with the symmetry constrained to C_{2v}. The frequency calculation (Table 4) results in only real vibrational frequencies, indicating that the equilibrium structure of the $A_1(n_y \rightarrow 3p_y)$ Rydberg state has C_{2v} symmetry. The optimized structure of the $A_1(n_y \rightarrow 3p_y)$ Rydberg state is shown in

Table 4. Calculated IR spectra of acetone in the $A_1(n_y \rightarrow 3p_y)$ and $B_2(n_y \rightarrow 3s)$ singlet excited states.[a]

Mode	Description	$A_1(n_y \rightarrow 3p_y)$		$B_2(n_y \rightarrow 3s)$		$B(n_y \rightarrow 3s)$	
		ν[b]	$\nu[D_6]/\nu[D_0]$	ν[b]	$\nu[D_6]/\nu[D_0]$	ν[b,c]	$\nu[D_6]/\nu[D_0]$
$\nu_1(a_1)$	CH stretch	3329 (3128)	0.743	3319	0.744	3318	0.744
$\nu_2(a_1)$	CH stretch	3189 (2424)	0.718 (0.739)	3146	0.717	3141	0.718
$\nu_3(a_1)$	C=O stretch	1704	0.974	1738	0.982	1739	0.982
$\nu_4(a_1)$	CH_3 deform	1564	0.743	1515	0.738	1517 (1232)	0.730 (0.763)
$\nu_5(a_1)$	CH_3 deform	1436 (1309)	0.759	1400	0.750	1402 (1191)	0.754 (0.760)
$\nu_6(a_1)$	CH_3 deform	1155 (1023)	0.809 (0.821)	1163	0.778	1159 (1047)	0.778 (0.783)
$\nu_7(a_1)$	CC stretch	769	0.922	672	0.948	668	0.944
$\nu_8(a_1)$	CCC scissor	352 (327)	0.852 (0.853)	332	0.871	331 (322)	0.871 (0.866)
$\nu_9(a_2)$	CH_3 stretch	3312	0.738	3223	0.741	3228	0.740
$\nu_{10}(a_2)$	CH_3 deform	1688	0.723	1556	0.722	1561	0.727
$\nu_{11}(a_2)$	CH_3 deform	948	0.746	1000	0.755	998	0.758
$\nu_{12}(a_2)$	disrot. torsion	61 (70)	0.618	− 104	0.711	120 (118)	0.711 (0.703)
$\nu_{13}(b_1)$	CH_3 stretch	3263	0.741	3473	0.738	3472	0.738
$\nu_{14}(b_1)$	CH_3 deform	1559	0.721	1591	0.779	1587	0.718
$\nu_{15}(b_1)$	CH_3 deform/CCO bend	1143	0.844	861	0.762	863	0.762
$\nu_{16}(b_1)$	CCO bend/CH_3 deform	419 (330)	0.848 (0.848)	1275	0.893	1275	0.973
$\nu_{17}(b_1)$	conrot. torsion	123	0.675	179	0.737	159 (175)	0.736 (0.754)
$\nu_{18}(b_2)$	CH stretch	3587	0.748	3331	0.742	3329	0.742
$\nu_{19}(b_2)$	CH stretch	3185	0.718	3142	0.717	3144	0.717
$\nu_{20}(b_2)$	CH_3 deform	1845	0.787	1550	0.731	1550	0.729
$\nu_{21}(b_2)$	CH_3 deform	1541	0.735	1444	0.750	1448	0.748
$\nu_{22}(b_2)$	CC stretch/CH_3 deform	1233	0.884	842	0.937	838	1.003
$\nu_{23}(b_2)$	CH_3 deform/CC stretch	995	0.794	1070	0.792	1079	0.741
$\nu_{24}(b_2)$	CCO bend	433	0.945	371	0.950	374	0.950

[a] The calculations are based on state-specific CASSCF calculations and the 6-311 + G(d,p) basis set, see text for details. [b] In cm^{-1}, experimental values (in parenthesis) are taken from ref. [19d]. [c] Note that the symmetry in this case is C_2, $\nu(a_1)$ and $\nu(a_2)$ correspond to $\nu(a)$ whereas $\nu(b_1)$ and $\nu(b_2)$ to $\nu(b)$.

Figure 4C. It is very similar to that of the ground state except that the CCC bending angle of the former is larger by $\sim 6°$.

The vibronic spectra of all the three 3p Rydberg states (A_1, A_2, and B_2) have been well studied and the vibrational progressions due to excitation to the $A_1(n_y \rightarrow 3p_y)$ Rydberg state have also been fully analyzed.[19d] Our ab initio results (Table 4) support most of the early spectroscopic assignments[19d] except those of the $\nu_2(a_1)$ and $\nu_{16}(b_1)$ modes, where the calculated frequencies differ by 32% and 27%, respectively. It was pointed out that the abnormal spectrum observed in the region of the $3p_y$ Rydberg state of acetone is probably due to vibrational coupling of this state with the $A_1(\pi \rightarrow \pi^*)$ valence state through the $\nu_2(a_1)$ CH stretching mode.[19d, 22] The issue of Rydberg–valence interaction arising from a nonadiabatic coupling between the $A_1(n_y \rightarrow 3p_y)$ Rydberg state and $A_1(\pi \rightarrow \pi^*)$ valence state of acetone will be further discussed in the following Sections.

2.2.3. The $A_1(\pi \rightarrow \pi^*)$ Valence State

As opposed to the Rydberg states discussed above, the structure of the symmetry-constrained minimum on the $A_1(\pi \rightarrow \pi^*)$ PES is dramatically different from the Franck–Condon (FC) species. This is mainly due to the $\pi \rightarrow \pi^*$ excitation character, where the perturbation of the CO π-bond strongly favors a longer CO bond. Therefore, the $A_1(\pi \rightarrow \pi^*)$ valence excited state (C_{2v}) was first characterized at the CAS(6,6)/6-311 + G(d,p) level from an initial geometry with long CO bond (for example, $r(CO) \sim 1.6$ Å). The MOs included in the active space of this CAS(6,6) calculation are similar to those used in predicting the vertical excitation energy of the same state at the CAS(6,5) level (Table 3) but with one

additional $p_x(b_1)$ orbital. Accordingly, the geometry of acetone in the $A_1(\pi \rightarrow \pi^*)$ state was optimized with the CO distance found to be 1.692 Å (Figure 5 A). However, a normal-mode analysis for this structure gives three imaginary frequencies, one corresponds to the out-of-plane CO wagging motion (b_1), while the other two correspond to symmetric and asymmetric CH_3 torsional motions (b_1, a_2); the corresponding vectors are shown in Figure 5 A.

Another ($\pi \rightarrow \pi^*$) stationary point with C_{2v} symmetry was found to have the staggered–staggered conformation (Figure 5 B) with only one imaginary frequency corresponding to the CO out-of-plane wagging motion (b_1). The minimum on the ($\pi \rightarrow \pi^*$) state is reached by relaxation of the C_{2v} geometry by destroying the (y, z) symmetry plane but still preserving the (x, z) symmetry plane. At the CAS(6,6)/6-311 + G(d,p) level the ($\pi \rightarrow \pi^*$) minimum is found to have C_s symmetry with a pyramidal angle (δ)[2] of 49° (Figure 5 C). Note that a frequency calculation has confirmed that the optimized species is a minimum (no imaginary frequencies). The calculated vibrational frequencies of each ($\pi \rightarrow \pi^*$) stationary points are shown in Table 5. Unfortunately, the IR spectrum of acetone in the ($\pi \rightarrow \pi^*$) state has yet to be determined experimentally so a comparison between theory and experiment cannot be made. The characteristics of the ($\pi \rightarrow \pi^*$) and the ($n_y \rightarrow \pi^*$)[2] excited states are similar.

2.2.4. The $B_1(n_z \rightarrow \pi^*)$ Valence State

The same strategy as for characterizing the ($\pi \rightarrow \pi^*$) excited state has been used to locate the equilibrium structure on the ($n_z \rightarrow \pi^*$) PES. The C_{2v} geometry of the ($n_z \rightarrow \pi^*$) excited state was
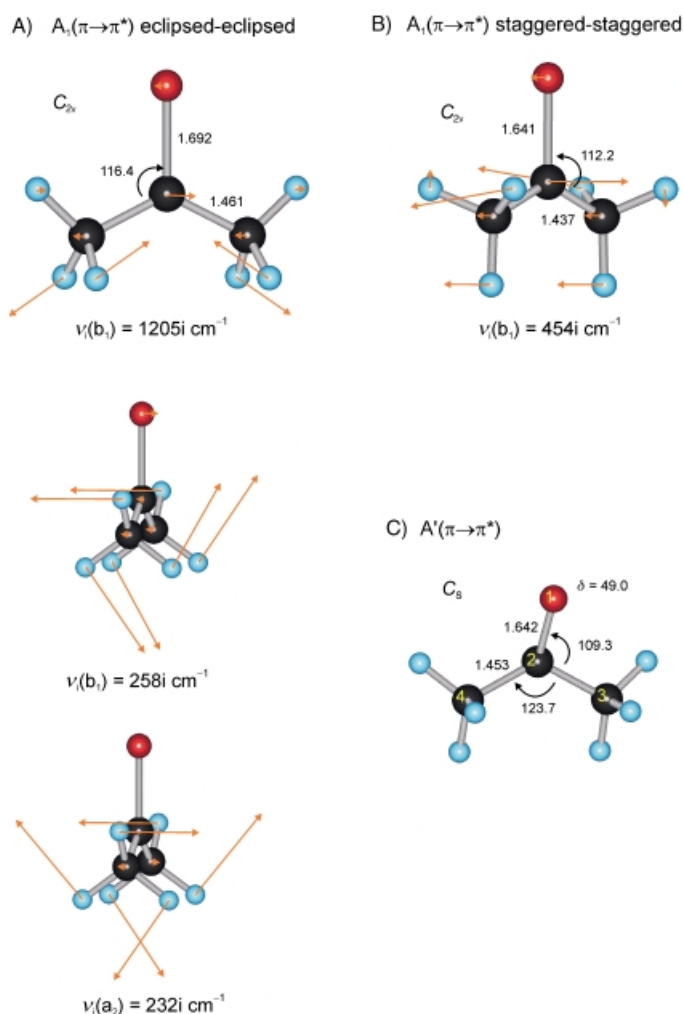
Figure 5. The structures and relevant geometrical parameters of A) the eclipsed – eclipsed $A_1(\pi \rightarrow \pi^*)$, B) the staggered – staggered $A_1(\pi \rightarrow \pi^*)$, and C) the pyramidal $A'(\pi \rightarrow \pi^*)$ species optimized at the CAS(6,6)/6-311 + G(d,p) level. The normal-coordinate vectors are shown as arrows and represent the nuclear motions corresponding to the imaginary frequencies of each species. The CO out-of-plane bending angle is defined as $\delta = 180° - D$, where D is the dihedral angle of $O_1C_2C_3C_4$.

successfully optimized at the CAS(6,5)/6-311 + G(d,p) level of theory. The optimized C_{2v} structures are shown in Figures 6A and 6B for the eclipsed – eclipsed and the staggered – staggered conformations, respectively. The most striking feature of the optimized structures of the $B_1(n_z \rightarrow \pi^*)$ valence state are the large CCC angles, which are predicted to be 137° and 140°, respectively. The CO distances of either of the $B_1(n_z \rightarrow \pi^*)$ optimized structures were determined to be 1.535 Å, which is in the middle range between the other two valence states of $r(CO) \sim 1.4$ Å for the $A_2(n_y \rightarrow \pi^*)$ state and ~ 1.7 Å for $A_1(\pi \rightarrow \pi^*)$. The vibrational frequency calculations indicate that the eclipsed – eclipsed conformation has two imaginary frequencies (the corresponding vectors are shown in Figure 6A) whereas the staggered – staggered conformation has only one imaginary value (the corresponding vector is shown in Figure 6B).

Attempts to locate a minimum on the $A'(n_z \rightarrow \pi^*)$ PES by relaxing the geometry from C_{2v} to $C_s(x, z)$ failed. This result was

reached in all attempts on the optimized structure on the $A'(\pi \rightarrow \pi^*)$ PES. The out-of-plane bending motion (b_1 mode) has effectively mixed both the A_1 and the B_1 states to have the same A' symmetry, therefore it is very difficult to distinguish between the $A'(n_z \rightarrow \pi^*)$ and the $A'(\pi \rightarrow \pi^*)$ states. We did not try to further locate the equilibrium structure for the next higher A' excited state but, instead, a series of surface-scan calculations along the CO stretching coordinate were carried out and the details are given in the following Section.

2.3. Topology Along the CO Stretching Coordinate

The one-dimensional potential energy curves along the CO bond-stretching coordinate of acetone have been reported by Merchán et al. for the first four singlet A_1 states (C_{2v} geometry) based on the CASPT2 method.[28] In the computational strategy of these authors, the potential curves corresponding to the S_0 and the other two A_1 Rydberg states were calculated as the first three roots for the CO distances shorter than 1.5 Å using the normal CAS(6,7) approach while the $(\pi \rightarrow \pi^*)$ potential curve was obtained separately throughout the whole $r(CO)$ region using a simplified CAS(4,4) approach; the latter approach is similar to our methodology in describing the $(\pi \rightarrow \pi^*)$ excitation as a second root of the CI equations (Table 3). Therefore, the interaction between the two A_1 Rydberg ($3p_y$, $3d_{yz}$) states and the $A_1(\pi \rightarrow \pi^*)$ valence state was not considered. As Merchán et al. pointed out, the avoided crossings at the region close to the curve-crossing points (shown in Figure 1 of ref. [28]) were "constructed by hand". We have reinvestigated the excited-state PESs of acetone not only for the A_1 excited states but also for the other relevant Rydberg and valence excited states as a function of the CO bond length using both the TDDFT and sa-CASSCF methods to describe the nature of the topology.

2.3.1. Time-Dependent DFT Calculations

Figure 7 shows the potential energy curves for various excited states of acetone (C_{2v}) along the CO bond-stretching coordinate. The potential energy curves were obtained in two steps. First, the geometry at each point on the PES was fully optimized along $r(CO)$ at the B3LYP/6-31 + G(d) level for the ground state. Second, single-point energy calculations at each optimized geometry of the ground-state surface were performed at the TD-B3LYP/6-31 + G(d) level of theory for prediction of the excitation energies of the excited states shown in Figure 7.

The excited-state PESs of acetone along the CO stretching coordinate shows several interesting features. The shapes of the PESs of all the 3s, 3p, and 3d Rydberg states are very similar to the shape of the ground state PES along $r(CO)$ with the minima located around 1.2 Å. In contrast, the PESs of all the valence excited states, including one A_1 state (blue curve in Figure 7), two A_2 states (orange curves), and two B_1 states (red curves), are more or less displaced from the ground-state PES along $r(CO)$. As a result, the Rydberg and the valence states cross extensively. From a dynamic point of view, the above theoretical finding shows that the excited acetone molecules can easily relax down to the lower states via the intermediate valence states,

Table 5. *Calculated IR spectra of eclipsed and staggered acetone in the $B_1(n_z \rightarrow \pi^*)$ and $A_1(\pi \rightarrow \pi^*)$ singlet excited states.[a]*

Mode	Description	$B_1(n_z \rightarrow \pi^*)$		$A_1(\pi \rightarrow \pi^*)$		$A'(\pi \rightarrow \pi^*)$
		ν[b]	ν[c]	ν[b]	ν[c]	ν[d]
$\nu_1(a_1)$	CH stretch	3309	3232	3294	3254	3269
$\nu_2(a_1)$	CH stretch	3148	3157	3105	3069	3048
$\nu_3(a_1)$	C=O stretch	1585	1615	1578	1567	1604
$\nu_4(a_1)$	CH$_3$ deform	1504	1516	1489	1500	1482
$\nu_5(a_1)$	CH$_3$ deform	1240	1190	1251	1295	1219
$\nu_6(a_1)$	CH$_3$ deform	862	878	977	923	906
$\nu_7(a_1)$	CC stretch	673	683	565	599	639
$\nu_8(a_1)$	CCC scissor	351	364	333	314	261
$\nu_9(a_2)$	CH$_3$ stretch	3200	3253	3130	3077	3204
$\nu_{10}(a_2)$	CH$_3$ deform	1576	1545	1570	1518	1524
$\nu_{11}(a_2)$	CH$_3$ deform	1054	1087	961	830	798
$\nu_{12}(a_2)$	disrot. torsion	− 184	188	− 232	339	336
$\nu_{13}(b_1)$	CH$_3$ stretch	3202	3254	3134	3076	3209
$\nu_{14}(b_1)$	CH$_3$ deform	1583	1574	1583	1510	1526
$\nu_{15}(b_1)$	CH$_3$ deform/CCO bend	1312	1078	575	1053	1174
$\nu_{16}(b_1)$	CCO bend/CH$_3$ deform	375	321	− 1205	− 455	440
$\nu_{17}(b_1)$	conrot. torsion	− 182	− 303	− 258	324	352
$\nu_{18}(b_2)$	CH stretch	3307	3228	3293	3249	3263
$\nu_{19}(b_2)$	CH stretch	3143	3145	3094	3054	3043
$\nu_{20}(b_2)$	CH$_3$ deform	1571	1601	1551	1626	1606
$\nu_{21}(b_2)$	CH$_3$ deform	1474	1481	1490	1460	1481
$\nu_{22}(b_2)$	CC stretch/CH$_3$ deform	1266	1387	1393	1371	1341
$\nu_{23}(b_2)$	CH$_3$ deform/CC stretch	1007	974	999	1058	1046
$\nu_{24}(b_2)$	CCO bend (ip)	462	412	314	270	238

[a] In cm^{-1}, the calculations are based on state-specific CASSCF calculations and the 6-311 + G(d,p) basis set, see text for details. [b] Eclipsed – eclipsed conformation. [c] Staggered – staggered conformation. [d] Note that the symmetry in this case is C_s, $\nu(a_1)$ and $\nu(b_1)$ correspond to $\nu(a')$ whereas $\nu(a_2)$ and $\nu(b_2)$ to $\nu(a'')$.
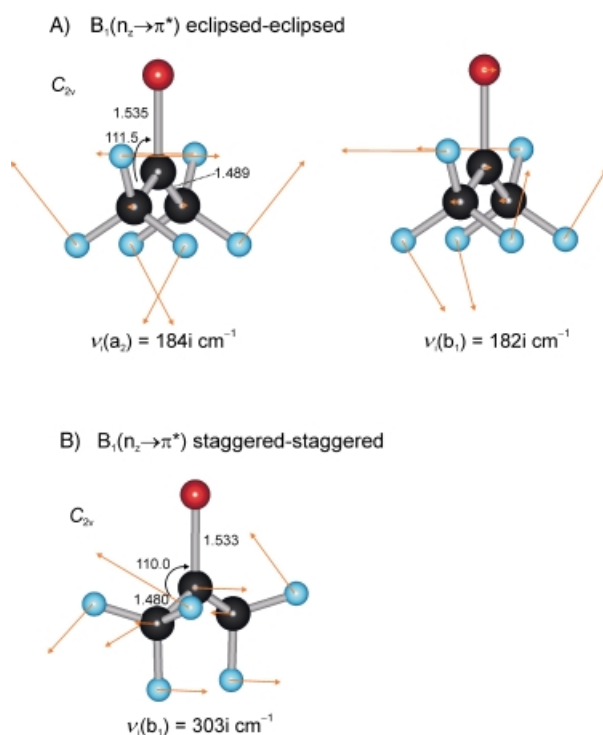

Figure 6. *The structures and geometrical parameters of A) the eclipsed – eclipsed $B_1(n_z \rightarrow \pi^*)$, and B) the staggered – staggered $B_1(n_z \rightarrow \pi^*)$ species optimized at the CAS(6,5)/6-311 + G(d,p) level. The normal-coordinate vectors are shown as arrows and represent the nuclear motions corresponding to the imaginary frequencies of each species.*
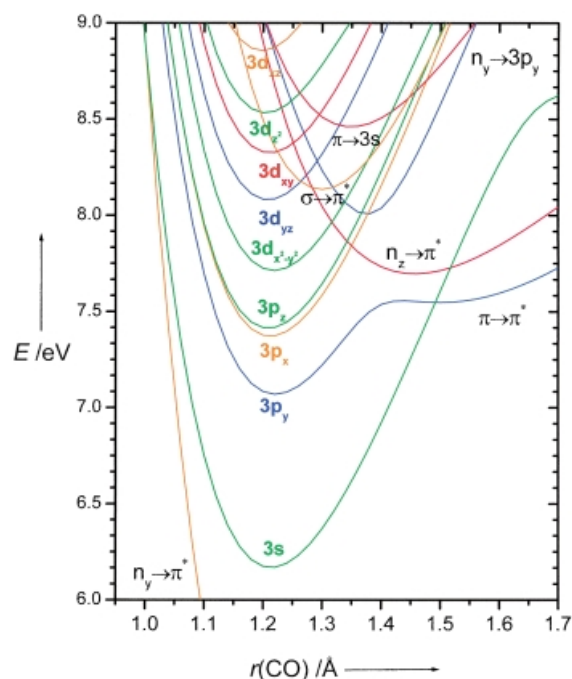

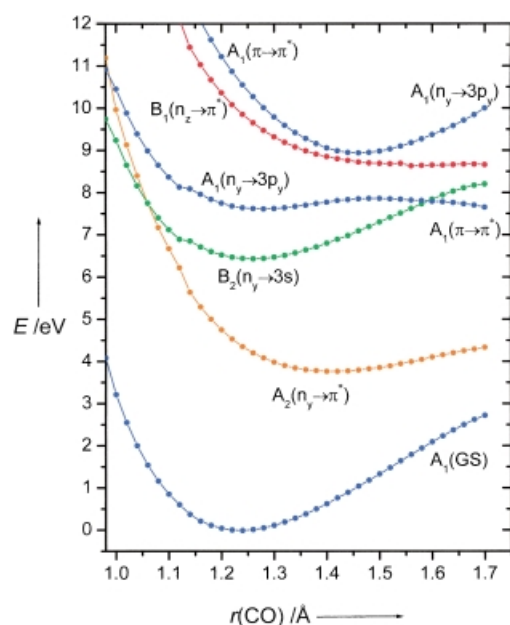**Figure 7.** *The excited-state potential energy curves of acetone along the r(CO) bond-stretching coordinate calculated at the TD-B3LYP/6-31 + G(d) level of theory. The calculated energies are relative to the S_0 minimum. The geometry at each point along the r(CO) coordinate was optimized at the B3LYP/6-31 + G(d) level for the ground state under constraint of C_{2v} symmetry. The states of different symmetry are represented by different colors: A_1 blue, A_2 orange, B_1 red, and B_2 green.*

most likely through either the $B_1(n_z \rightarrow \pi^*)$ or the $A_1(\pi \rightarrow \pi^*)$ state along the $r(CO)$ coordinate. Furthermore, strong coupling between the $A_1(n_y \rightarrow 3p_y)$ Rydberg and the $A_1(\pi \rightarrow \pi^*)$ valence states leads to an avoided-crossing point between these two potential curves at longer CO distance (~ 1.4 Å). At still longer distances, the $B_2(n_y \rightarrow 3s)$ Rydberg curve crosses the $A_1(\pi \rightarrow \pi^*)$ and subsequently the $B_1(n_z \rightarrow \pi^*)$ valence curves at $r(CO) \sim 1.5$ Å. At a shorter CO distance (~ 1.05 Å), a curve-crossing point between the $B_2(n_y \rightarrow 3s)$ Rydberg and the $A_2(n_y \rightarrow \pi^*)$ valence states has also been found, which could open a relaxation channel for excited-state acetone to further go down in energy to the lowest singlet excited state ($S_2 \rightarrow S_1$). To further investigate these features, we have carried out sa-CASSCF calculations for the relevant excited-state potential energy curves of acetone.

2.3.2. State-Averaged CASSCF Calculations

The excited-state PESs of acetone along the CO bond-stretching coordinate have also been characterized using the state-averaged CASSCF approach at the CAS(6,7)/6-311 + G(d,p) level of theory. Prior to the surface scan, calculations were performed at the FC geometry to assure that the MOs have been adequately chosen so that the active space can describe all the states of interest. The potential energy curves calculated for the two relevant Rydberg states ($B_2(n_y \rightarrow 3s)$ and $A_1(n_y \rightarrow 3p_y)$) and the three valence states ($A_2(n_y \rightarrow \pi^*)$, $B_1(n_z \rightarrow \pi^*)$, and $A_1(\pi \rightarrow \pi^*)$) are shown in Figure 8. Note that the excited-state PESs of acetone discussed previously based on the TDDFT approach (Figure 7) are qualitatively the same as the sa-CASSCF results (Figure 8).

Figure 8. *The ground-state and five excited-state potential energy curves of acetone along the r(CO) bond-stretching coordinate calculated at the state-averaged CAS(6,7)/6-311 + G(d,p) level of theory. The geometry at each point along the r(CO) coordinate was optimized at the B3LYP/6-31 + G(d) level for the ground state under constraint of C_{2v} symmetry. The states of different symmetry are represented by colors: A_1 blue, A_2 orange, B_1 red, and B_2 green.*

As discussed in Section 2.2, the optimized geometry relating to the Rydberg state has a planar CCCO structure (either C_{2v} or C_2) whereas that of a valence excited state has a nonplanar structure (C_s) with the CO moiety bent out of the molecular symmetry plane (see Figures 4 – 6). The out-of-plane bent (pyramidal) feature of a valence excited state can be rationalized as arising from an excitation involving an antibonding (π^*) orbital. Within the framework of a simple VB model, this causes the p_x orbital of the central carbon atom to be included into the hybridization resulting in an sp³-type carbon atom. Therefore, from the FC region along the CO out-of-plane bending coordinate, one would expect that the excited acetone molecule will go uphill onto a Rydberg PES but downhill onto a valence PES.

In Figure 9, we show the calculated excited-state potential curves of acetone along the CO bond-stretching coordinate based on the nonplanar structures (C_s) that result from a scan of the $A'(\pi \rightarrow \pi^*)$ surface. The potential energy for the Rydberg states and the valence excited states change in opposite
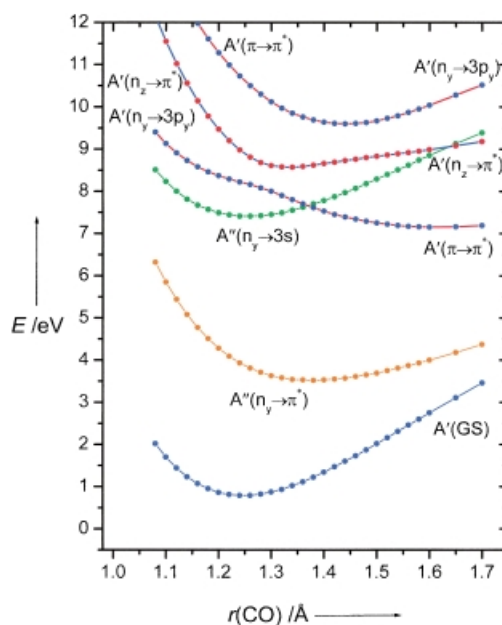
Figure 9. *The excited-state potential energy curves of acetone along the r(CO) bond-stretching coordinate calculated at the state-averaged CAS(6,7)/6-311 + G(d,p) level of theory. The geometry at each point along the r(CO) coordinate was optimized at the CAS(8,8)/cc-pVDZ level for the $\pi \rightarrow \pi^*$ excited state under constraint of C_s symmetry. The coupling between the $A'(n_z \rightarrow \pi^*)$, $A'(n_y \rightarrow 3p_y)$, and the $A'(\pi \rightarrow \pi^*)$ states is indicated by the colors of the markers for the calculated points and the lines that connect them.*

directions upon the relaxation from C_{2v} to C_s symmetry. Therefore, the $A''(n_y \rightarrow 3s)$ potential curve no longer crosses that of the $A''(n_y \rightarrow \pi^*)$ at short CO distances, and the curve-crossing point between the $A''(n_y \rightarrow 3s)$ state and the $A'(\pi \rightarrow \pi^*)$ state now occurs at shorter distances. The $B_1(n_z \rightarrow \pi^*)$ and $A_1(\pi \rightarrow \pi^*)$ states transform to $A'(n_z \rightarrow \pi^*)$ and the $A'(\pi \rightarrow \pi^*)$ when the symmetry is lowered from C_{2v} to C_s. The $A'(n_z \rightarrow \pi^*)$ and the $A'(\pi \rightarrow \pi^*)$ valence states are substantially mixed with the $A'(n_y \rightarrow 3p_y)$ Rydberg state ($r(CO) \sim 1.3$ Å, Figure 9). This indicates that the Rydberg – valence

interaction can be described at the CI level when a reasonably sized active space is employed.

The one-dimensional surface-scan results shown in Figures 8 and 9 indicate the existence of many conical intersections which play key roles in affecting the dynamic behavior of the process taking place on the excited-state PES of acetone. With the guidance of those surface-scan calculations, we have successfully located the central conical intersections (**CI**s) by searching for the lowermost point along the crossing seam of two intersecting surfaces. The results are presented in the following Section.

2.4. Conical Intersections and Avoided Crossings

From a fundamental quantum-mechanical point of view, two PESs of a diatomic molecule will intersect *only if* the two states have a different symmetry; in other words, an avoided crossing would result if two PESs of a diatomic molecule have the same symmetry.[36, 37] However, this "noncrossing rule" criterion is no longer valid for a polyatomic molecule—in that case two PESs can in principle intersect *even if* they belong to the same symmetry group, thus leading to a conical intersection between the two intersecting surfaces.[37]

The conical intersection has been recognized as a "photochemical funnel" to play a key role in many photoinduced reactions.[36–43] Since the process of funneling through a **CI** is very efficient, the nonradiative decay from the upper surface to the lower one usually occurs within a single vibrational period.[42, 43] Furthermore, the structural information of a **CI** may provide significant insight into the mechanism of product formation from a "photochemically heated" ground-state species.[2, 43, 44] Schematically, the bifurcated character (with respect to the gradient difference (x_1) and nonadiabatic coupling (x_2) vectors) of a **CI** can be represented by a single crossing point of a double cone formed by two intersecting surfaces along the $(n-2)$-dimensional hyperline, where n is the number of the degrees of freedom in the molecule. The remaining two coordinates are related to the x_1 and x_2 vectors, which define the branching space. A detailed review regarding the computational strategy to characterize conical intersections for many typical photochemical reactions is given in ref. [37]. Using a similar approach as detailed previously,[37] we have successfully located the exact position for the conical intersections (or avoided crossing (**AC**) if the two surfaces do not intersect), which may be essential in describing the experimentally observed ultrafast dynamics upon excitation to the high-energy excited-state PESs of acetone[3a, 29] and other ketones.[45]

2.4.1. The *CI* Between the $B_2(n_y \rightarrow 3s)$ Rydberg and the $A_2(n_y \rightarrow \pi^*)$ Valence States (*CI1*)

The surface-scan calculations shown in Figure 8 guide the search for a conical intersection between the $B_2(n_y \rightarrow 3s)$ Rydberg and the $A_2(n_y \rightarrow \pi^*)$ valence states in the sense that an initial geometry with $r(CO) = 1.06$ Å was employed. Several different sets of MOs were tested at this initial geometry, and the final active space was chosen to have six electrons in a total of seven

orbitals, where for the ground state the six electrons are occupying the $\sigma(b_2)$, $\pi(b_1)$, and $n_y(b_2)$ MOs and the other four virtual orbitals are the $\pi^*(b_1)$, $3s(a_1)$, $p_y(b_2)$, and $p_z(a_1)$ MOs. Using the specified sa-CAS(6,7) approach with the 6-311 + G(d,p) basis set, the $A_2(n_y \rightarrow \pi^*)$ and the $B_2(n_y \rightarrow 3s)$ states were calculated to be the second and the third roots of the solution in the initial calculation, respectively, with the energy gap between the two states predicted to be 0.34 eV. The geometry optimization of **CI1** was carried out using the method implemented in Gaussian 98.[46] Eventually, the total energy of **CI1** was determined to be -191.79322 hartree with the energy gap between the two states of less than 10^{-5} hartree.

The optimized geometry and the corresponding x_1 and x_2 vectors of **CI1** are shown in Figure 10 A. Two points are particularly worth mentioning. First, the CO bond is short (1.073 Å) and the CCO bond angle is wide (126.5°). Furthermore, the two equivalent CC bonds in **CI1** are considerably longer than in the FC geometry (1.640 versus 1.518 Å). Second, the nuclear motions imposed by the x_1 and x_2 vectors guide the consecutive reaction paths on the lower-energy surface after the passing of **CI1**. As shown in Figure 10 A, x_1 corresponds to the CO stretching motion (a_1 mode) whereas x_2 relates to the CO out-of-plane
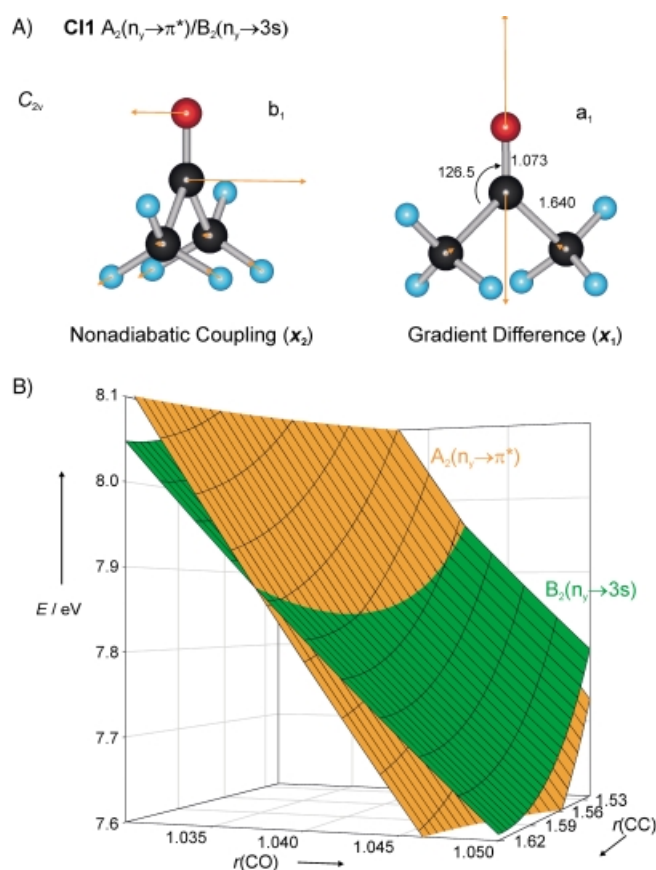

Figure 10. A) The structure and geometrical parameters of the S_1/S_2 conical intersection (*CI1*) optimized at the CAS(6,7)/6-311 + G(d,p) level. The nonadiabatic coupling (x_2) and the gradient difference (x_1) vectors are shown as arrows. B) The $S_1(n,\pi^*)$ and the $S_2(n,3s)$ PESs calculated at the TD-B3LYP/6-31 + G(d) level of theory along the r(CO) and the r(CC) stretching coordinates. Note for the seam formed by the two intersecting surfaces, its the lowest point is located at r(CO) = 1.04 and r(CC) = 1.58 Å.

bending motion (b_1 mode). When the molecule proceeds in the x_1 and x_2 directions on the S_1 surface, it will reach the S_1 minimum region at $r(CO) \sim 1.4$ Å. Note that the CO bond could dissociate on the S_1 surface along the x_1 vector. However, the energy demand for this reaction is substantial (~ 6 eV above the S_0 minimum) and it will not be considered any further.

Conical intersections can be divided into three classes based on their topology.[37] We note that **CI1** is a sloped **CI**, which involves an uphill path (without a saddle point). The funneling through a sloped **CI** is relatively slow and resembles more closely a process with an energy barrier.[37] To further demonstrate this sloped **CI** feature for **CI1**, we have carried out two-dimensional surface-scan calculations using the TDDFT approach. The 2D PESs of acetone were calculated at the TD-B3LYP/6-31 + G(d) level along both the CO bond-stretch and the synchronous CC bond-stretch coordinates with the remaining coordinates fixed according to **CI1** (Figure 10 A) and retaining the C_{2v} symmetry throughout the calculations. The results for the $A_2(n_y \rightarrow \pi^*)$ and $B_2(n_y \rightarrow 3s)$ surfaces (orange and green) are shown in Figure 10 B; the seam between the two intersecting surfaces can be seen. The minimum-energy point on this seam is found for a CO bond length of 1.04 Å and a CC bond length of 1.58 Å. Note that the geometry of the **CI1** estimated by the TDDFT method has a shorter CO distance than that predicted by the CASSCF approach, which could be the reason why the energy relative to the ground state is higher for the former.

2.4.2. The *CI* Between the $B_2(n_y \rightarrow 3s)$ Rydberg and the $A_1(\pi \rightarrow \pi^*)$ Valence States (*CI2*)

Section 2.4.1 focused on characterizing **CI1** as the lowest crossing point between the $B_2(n_y \rightarrow 3s)$ and the $A_2(n_y \rightarrow \pi^*)$ states at a short CO distance. As suggested by the surface-scan calculations shown in Figure 8, we now discuss the features of the lowest crossing point (**CI2**) between the $B_2(n_y \rightarrow 3s)$ and the $A_1(\pi \rightarrow \pi^*)$ states, found at a long CO distance.

An active space was chosen to have six electrons in seven orbitals, where for the first root (ground state) the six electrons occupy the $n_z(a_1)$, $\pi(b_1)$, and $n_y(b_2)$ MOs and the four virtual orbitals are the $\pi^*(b_1)$, $3s(a_1)$, $p_y(b_2)$, and $p_z(a_1)$ MOs. Using a guess geometry where $r(CO) = 1.46$ Å, the $B_2(n_y \rightarrow 3s)$ and the $A_1(\pi \rightarrow \pi^*)$ states were calculated to be the third and the fourth roots in the specified sa-CAS(6,7) calculation with the 6-311 + G(d,p) basis set, respectively. Similar to the procedure for characterizing **CI1**, the geometry of **CI2** was optimized and the total energy was determined to be -191.79943 hartree with the energy gap between the two states of less than 10^{-6} hartree.

The optimized structure and the corresponding x_1 and x_2 vectors of **CI2** are shown in Figure 11. The geometry of **CI2** differs from that of **CI1** with respect to both CO and CC distances. The CO distance in **CI2** is much longer than in **CI1** (1.496 versus 1.073 Å), whereas the CC distance is smaller (1.467 versus 1.640 Å). Furthermore, the CCO angle of **CI2** is smaller than that of **CI1** by 8.5°. Note that the values of the three geometrical parameters at the FC geometry are in between those of **CI1** and **CI2**. From a dynamic point of view, the gradient difference vector
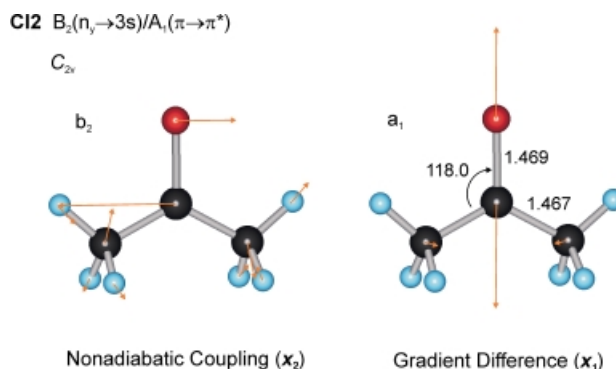

CI2 $B_2(n_y \rightarrow 3s)/A_1(\pi \rightarrow \pi^*)$

Figure 11. The structure and geometrical parameters of the $B_2(n_y \rightarrow 3s)/A_1(\pi \rightarrow \pi^*)$ conical intersection (**CI2**) optimized at the CAS(6,7)/6-311 + G(d,p) level. The nonadiabatic coupling (x_2) and the gradient difference (x_1) vectors are shown as arrows.

(x_1) of **CI2** corresponds to the CO stretching motion (a_1 mode) similar to that of **CI1**; however, the nonadiabatic coupling vector (x_2) of **CI2** gives an in-plane CCO bending/asymmetric CC stretching motion corresponding to a b_2 vibrational mode perpendicular to the x_2 vector of **CI1**. Note that the vibrational mode (Q) of the x_2 vector must belong to the B_2 irreducible representation in order for the matrix element $\langle B_2 | Q | A_1 \rangle$ relating to **CI2** to have a component of the total-symmetric irreducible representation.

CI2 is not sloped (as was the case for **CI1**, Figure 8). The curve crossing through **CI2** will either result in vibrationally excited species (left side of the lower $B_2(n_y \rightarrow 3s)$ surface state) or lead to the formation of acetone molecules in the $A_1(\pi \rightarrow \pi^*)$ state (when proceeding to the right). Accordingly, if the x_1 vector is followed from the **CI2** geometry in the direction of shorter CO distance, **CI1** may be reached after having passed through the minimum region of the $B_2(n_y \rightarrow 3s)$ surface. However, the other direction of the x_1 vector points towards lengthening the CO bond, which may eventually result in breakage of the CO bond but the energy demand is substantial (~ 8 eV above the S_0 minimum). The forward and the reverse direction of the x_2 vector will guide towards a prompt, nonconcerted α-CC bond-cleavage process on the S_2 (3s Rydberg) PES. We further discuss the Norrish type-I reaction of acetone occurring on the S_2 surface in Section 2.5.

2.4.3. The *CI* Between the $B_2(n_y \rightarrow 3s)$ Rydberg and the $B_1(n_z \rightarrow \pi^*)$ Valence States (*CI3*)

The search for a conical intersection (**CI3**) between the $B_2(n_y \rightarrow 3s)$ and the $B_1(n_z \rightarrow \pi^*)$ surfaces has been performed using a strategy similar to that of the two previous Sections. The active space was chosen to have six electrons distributed among six orbitals. Since we are not interested in the $A_1(\pi \rightarrow \pi^*)$ state, the $\pi(b_1)$ MO is omitted from the active space and the CAS includes the following MOs: $n_z(a_1)$, $n_z'(a_1)$, $n_y(b_2)$, $\pi^*(b_1)$, $3s(a_1)$, and $p_z(a_1)$. This choice of active space ensures that the $B_2(n_y \rightarrow 3s)$ and the $B_1(n_z \rightarrow \pi^*)$ states appear in the configuration-interaction solution to be the third and the fourth roots. Starting from a

geometry similar to **CI2**, the geometry of **CI3** was optimized at the specified sa-CAS(6,6) level with the 6-311 + G(d,p) basis set.

The optimized structure and the corresponding x_1 and x_2 vectors of **CI3** are shown in Figure 12. The CO distance of **CI3** is even longer (1.532 Å). The CCO bending angle is 110.0°, which is much smaller than that in **CI2**. We notice that the structure of **CI3**
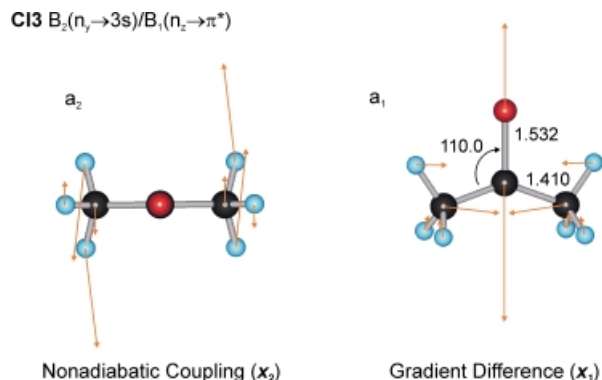

Figure 12. *The structure and geometrical parameters of the $B_2(n_y \rightarrow 3s)/$ $B_1(n_z \rightarrow \pi^*)$ conical intersection (**CI3**) optimized at the CAS(6,6)/6-311 + G(d,p) level. The nonadiabatic coupling ($\mathbf{x_2}$) and the gradient difference ($\mathbf{x_1}$) vectors are shown as arrows.*

is somewhat similar to the one calculated for the $B_1(n_z \rightarrow \pi^*)$ minimum under the constraint of C_{2v} symmetry (Figure 6 A) except that the CC bond length is shorter by ~0.08 Å in the former. The nuclear motion following the x_1 vector direction of **CI3** corresponds to an a_1 CO stretching vibration (Figure 12), which is analogous to both **CI1** and **CI2** shown in Figures 10 A and 11, respectively. However, the dynamic feature of **CI3** is different from that of **CI1** and **CI2**, since the nuclear motion following the x_2 vector direction for **CI3** is related to an asymmetric CH_3 torsional motion with a_2 symmetry. Indeed, not only the structures and the energetics but also the dynamic features (torsional motions being activated) are very similar for **CI3** and the $B_1(n_z \rightarrow \pi^*)$ symmetry-constrained minimum. This is consistent with the surface-scan results shown in Figure 7, which indicate that the $B_1(n_z \rightarrow \pi^*)$ symmetry-constrained minimum (Figure 6) is located very close to **CI3**.

2.4.4. The Avoided Crossing Between the $A_1(n_y \rightarrow 3p_y)$ Rydberg and the $A_1(\pi \rightarrow \pi^*)$ Valence States (AC1)

We show in Figures 7 and 8 that the second A_1 state of acetone is a 3p Rydberg state at short CO distances but its character changes to a $(\pi \rightarrow \pi^*)$ valence state at long CO distances. This feature have been pointed out by Merchán et al.[28] However, instead of a true curve crossing or a weak avoided crossing, a strong avoided crossing between the second and the third A_1 states unambiguously emerges from our surface-scan calculations using both the TDDFT and the CASSCF methods. Therefore, we have embarked on an optimization of the geometry for the avoided-crossing point between the two A_1 states.

The strategy of choosing an appropriate set of MOs in optimizing the structure for the AC ($AC1$) between the

$A_1(n_y \rightarrow 3p_y)$ Rydberg and the $A_1(\pi \rightarrow \pi^*)$ valence states is to place the $3p_y(b_2)$ orbital in and leave the $3s(a_1)$ orbital out of the active space. Thus, in the CAS(6,7)/6-311 + G(d,p) calculation the chosen active space involves six electrons distributed among the $n_z(a_1)$, $\pi(b_1)$, $n_y(b_2)$, $\pi^*(b_1)$, $3p_y(b_2)$, $p_y(b_2)$, and $p_z(a_1)$ orbitals. This choice of active space ensures that the contributions from both $A_1(n_y \rightarrow 3p_y)$ and $A_1(\pi \rightarrow \pi^*)$ states appear in both the third and the fourth roots of the configuration-interaction solution at the initial geometry of $r(CO) \sim 1.4$ Å, while the first root gives the mixed configurations of the ground state and the $(\pi \rightarrow \pi^*)$ state and the second root corresponds to a nearly pure $A_2(n_y \rightarrow \pi^*)$ state.

Our initial attempts to optimize the geometry show that the two in-plane CH bond distances must be fixed, otherwise a synchronous dissociation of the two CH bonds follows when the energy gap between the states corresponding to the third and the fourth roots is minimized.[47] The in-plane CH bond length was frozen at 1.086 Å whereas the rest of the parameters were optimized with respect to the energy of the state corresponding to the fourth root under the constraint of C_{2v} symmetry. Eventually, the partially optimized $AC1$ structure was found, and the energy of the third and the fourth root is − 191.77385 and − 191.75593 hartree, respectively, with the energy gap between the two roots predicted to be 0.49 eV.

The optimized structure and the corresponding x_1 and x_2 vectors of $AC1$ are shown in Figure 13. Both the gradient difference and the nonadiabatic coupling vectors correspond to
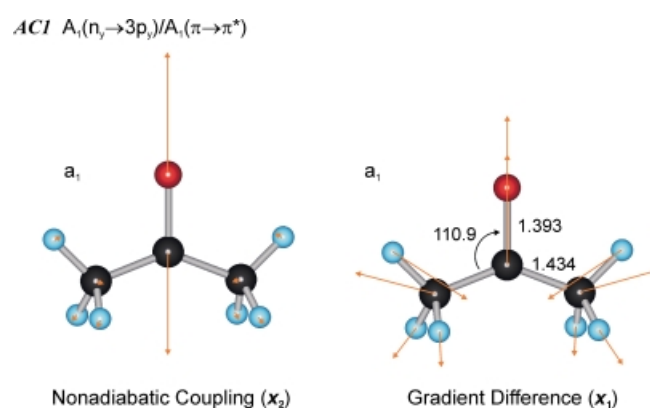

Figure 13. *The structure and geometrical parameters of the $A_1(n_y \rightarrow 3p_y)/$ $A_1(\pi \rightarrow \pi^*)$ avoided crossing (**AC1**) partially optimized at the CAS(6,7)/6-311 + G(d,p) level. The nonadiabatic coupling ($\mathbf{x_2}$) and the gradient difference ($\mathbf{x_1}$) vectors are shown as arrows.*

the CO stretching motion with a_1 symmetry. This dynamic feature is consistent with the surface-scan calculations (Figure 8). In other words, the intrinsic avoided crossing between the two A_1 excited states has led to an energy barrier on the second A_1 surface for acetone, where the left side (shorter CO distance) of the surface corresponds to the $3p_y$ Rydberg state while the right side (longer CO distance) of the surface corresponds to the $(\pi \rightarrow \pi^*)$ valence state. Our theoretical finding indicates that there is a substantial Rydberg–valence interaction between the $A_1(n_y \rightarrow 3p_y)$ Rydberg state and the $A_1(\pi \rightarrow \pi^*)$ valence state, due

to the strong nonadiabatic coupling (the a_1 CO stretching mode) between the two states, as has been suggested earlier on the basis of spectroscopic results.[22]

2.4.5. Other CIs Between the 3s Rydberg and the ($\pi \rightarrow \pi^*$) Valence States

In the above Sections, we have addressed the structural and the dynamic features of excited-state acetone in the C_{2v} eclipsed – eclipsed conformation (Figures 5 A and 6 A) through the characterization of three conical intersections along the $B_2(n_y \rightarrow 3s)$ surface and one avoided crossing between the two A_1 excited states. The results for **CI1**, **CI2**, **CI3**, and **AC1** are consistent with what might have been anticipated from the 1D surface-scan results shown in Figures 7 and 8. Among all the curve-crossing and avoided-crossing points we have studied, **CI2** is central because its dynamic driving force determines the subsequent reaction path to be followed on the S_2 surface. Therefore, we have further investigated the **CI**s similar to **CI2** but with different conformations. First we consider the effect of the two CH_3 torsional motions, which led to a C_{2v} staggered – staggered conformer for **CI2**. Second, the CO out-of-plane bending motion has been taken into account, which has effectively changed the symmetry of the **CI2** structure from C_{2v} to C_s. A strategy similar to searching for **CI2** has been employed, and the two optimized structures and their corresponding x_1 and x_2 vectors are shown in Figures 14 and 15 A. A schematic representation for the possible reaction paths and their corresponding intermediates (products) of funneling through the bent **CI2** (C_s) is illustrated in Figure 15 B.
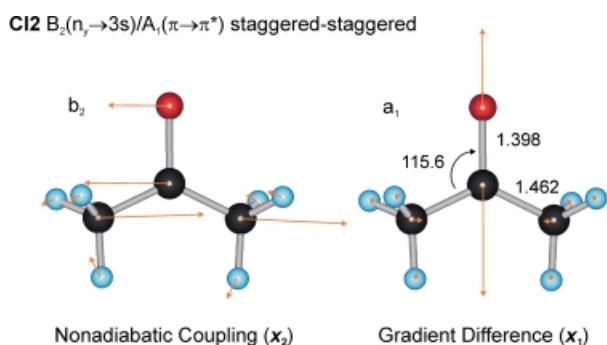

CI2 $B_2(n_y \rightarrow 3s)/A_1(\pi \rightarrow \pi^*)$ staggered-staggered

Figure 14. *The staggered – staggered conformation of the $B_2(n_y \rightarrow 3s)/A_1(\pi \rightarrow \pi^*)$ conical intersection optimized at the CAS(6,7)/6-311 + G(d,p) level. The nonadiabatic coupling (x_2) and the gradient difference (x_1) vectors are shown as arrows.*

2.5. α-CC Bond-Breaking Reaction Pathways of Acetone

Our previous results and discussion indicate that the α-cleavage in acetone can occur on the S_2 (3s Rydberg) surface; it is driven by the nonadiabatic coupling dynamics of **CI2** when the molecule has been excited to a high-energy Rydberg state. Figure 15 B shows the nuclear motion that would result when the x_2 vector is followed; it can be seen that it lead to α-CC bond cleavage on the S_2 PES. The following two questions are
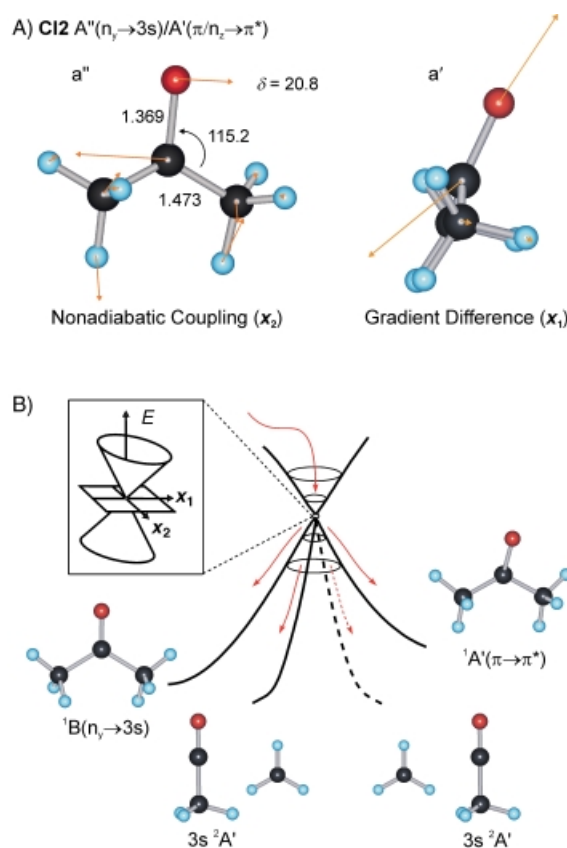

Figure 15. *A) The structure and geometrical parameters of the $A''(n_y \rightarrow 3s)/A'(\pi \rightarrow \pi^*)$ conical intersection (CI2) optimized at the CAS(6,7)/6-311 + G(d,p) level of theory. The nonadiabatic coupling (x_2) and the gradient difference (x_1) vectors are shown as arrows. B) Branching at CI2. In the gradient difference vector (x_1) direction, the product will be acetone in either the ($n_y \rightarrow 3s$) or the ($\pi \rightarrow \pi^*$) excited state. In the nonadiabatic coupling vector (x_2) direction, the asymmetric CC-stretching motion becomes activated, which leads to the α-cleavage on the 3s PES to form the linear excited-state (3s $^2A'$) acetyl radical.*

pertinent: a) How high is the reaction barrier along the α-cleavage RC on the S_2 PES of acetone? b) What are the electronic and the nuclear structures of the intermediates and what are the end products of the reaction? To answer these questions, we have characterized the S_2 PES of acetone along the α-CC bond-breaking RC using both the TDDFT and the CASSCF methods, and the details are given in the following Sections.

2.5.1. A Two-Dimensional Presentation of the α-Cleavage on the 3s PES

Figure 16 shows the 3s Rydberg PES of acetone along both the α-CC bond-breaking and the CCO bending coordinates. The 2D calculations were performed at the TD-B3LYP/6-31 + G(d) level with the geometry at each point optimized for the ground state of the cation, since one might anticipate a close resemblance between the cation and the Rydberg-state geometries. Such a 2D surface scan provides an estimate of the minimum-energy pathway (MEP) for the α-cleavage bond-dissociation channel of acetone on the 3s surface. This partly answers the two questions. First, at the TD-B3LYP/6-31 + G(d) level of theory, the energy
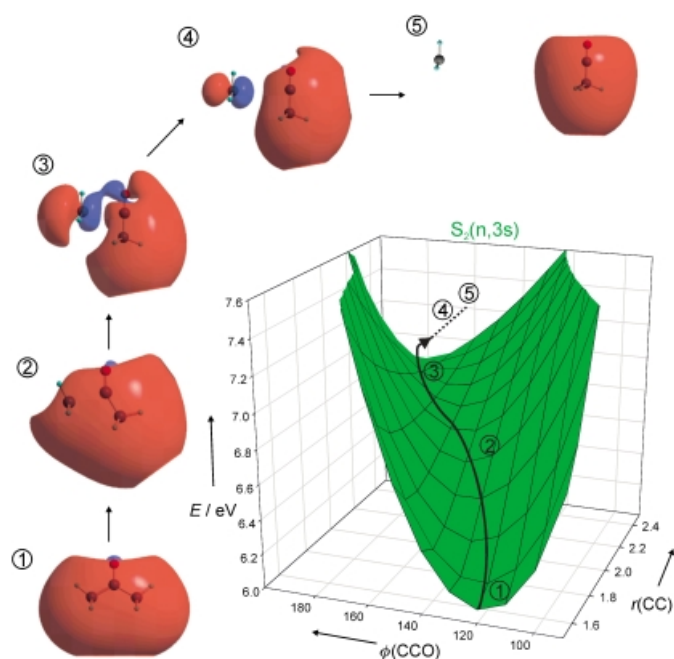
Figure 16. *The $S_2(n,3s)$ PES of acetone calculated at the TD-B3LYP/6-31 + G(d) level of theory along the r(CC) stretching and the ϕ(CCO) bending coordinates the constraint of C_s symmetry with respect to the (y, z) plane. The molecular structures together with the corresponding 3s Rydberg orbitals are shown for the MEP at r(CC) = 1.5, 2.0, 2.5, 3.5, and 6.0 Å, respectively.*

barrier for the α-CC bond breakage of acetone occurring on the 3s PES is predicted to be less than 1.0 eV (6.9 eV above the ground-state equilibrium geometry). Second, the change of the geometry along the α-cleavage MEP is significant, in particular the CCO bond angle increases to yield a linear geometry along the MEP to dissociation. A survey of the MOs along the MEP (Figure 16) indicates that the α-cleavage of a 3s acetone (S_2) actually leads to a 3s acetyl radical and a ground-state methyl radical, Equation (1).

$$CH_3COCH_3\ (S_2)\ \xrightarrow{\textbf{TS1}}\ CH_3CO^\bullet\ (3s\ ^2A') + CH_3^\bullet\ (\tilde{X}^2A_2'') \qquad (1)$$
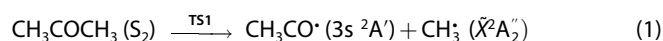
We now further test the validity of this mechanism using the ss-CASSCF approach.

2.5.2. The Transition State *(TS1) on the S_2 (3s Rydberg) Surface*

Based on the TDDFT surface-scan results shown in Figure 16, we start the ss-CASSCF calculations from a geometry with r(CC) = 2.2 Å and ϕ(CCO) = 165°. The active space is chosen to have six electrons in the following seven MOs: σ(a'), π(a''), n_y(a'), 3s(a'), σ*(a'), σ'*(a'), and p_x(a''). Note that only the (y, z) symmetry plane (C_s symmetry) was retained throughout the calculations so that the original a$_1$- and b$_2$-type MOs of C_{2v} symmetry are now reduced to the a'-type MOs; b$_1$- and a$_2$-type MOs are reduced to the a''-type MOs. The result of the ss-CAS(6,7) calculations are shown in Figure 17. It can be seen that the initial n_y(a') and the 3s(a') MOs couple strongly. This behavior is very similar to that of the A$_1$($n_y \rightarrow 3p_y$) state (Section 2.1.4). Similarly, the Rydberg – valence coupling between the A'($n_y \rightarrow 3s$) and the A'($n_y \rightarrow \sigma$*) states

could be significant at longer α-CC distances, since our calculations have indicated that a substantial σ-antibonding character is involved in the half-broken CC bond of acetone shown in the $n_y + 3s$ (a') MO (Figure 17).

The geometry optimization at the CAS(6,7)/6-311 + G(d,p) level of theory lead to the α-cleavage saddle point (**TS1**) of C_s symmetry; the structure and the vector corresponding to the imaginary frequency (865i cm^{-1}) and the subsequent IRC results[48] are also shown in Figure 17. The structure of **TS1** has a characteristic geometric feature with the α-CC bond distance (reaction coordinate, RC) determined to be 2.045 Å together with a short CO bond length (1.133 Å) and a wide CCO bond angle (149.6°). Following the imaginary mode in the forward direction the CCO angle opens and the molecule becomes linear; at the last converged intrinsic reaction coordinate point (r(CC) = 2.33 Å), the CCO angle is 167.2° and the CO bond length decreased to 1.116 Å. This shows that the linear 3s acetyl radical is the product of the α-CC bond-breaking reaction of acetone. To overcome the difficulties encountered in the calculations at large CC separations, we shall characterize the excited-state PESs for the acetyl radical; the results are presented in Section 2.6.
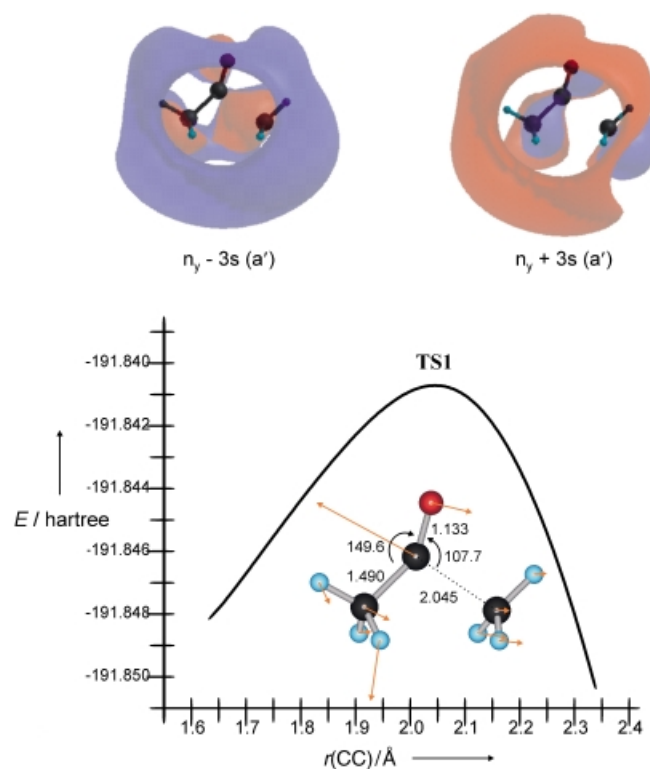

Figure 17. *The structure, central MOs, and the corresponding IRC path of the α-cleavage transition state (**TS1**) on the ($n_y \rightarrow 3s$) PES optimized at the CAS(6,7)/6-311 + G(d,p) level of theory. The depicted normal-coordinate vector represents the nuclear motion corresponding to the imaginary frequency, which is related to the α-cleavage process.*

2.5.3. TDDFT Scans along other Coordinates

To show the uniqueness in the property of the PES along the CO stretching, the CC stretching, and the CCO bending coordinates, four additional surface-scan calculations have been carried out

at the TD-B3LYP/6-31 + G(d) level. The coordinates in question are the CH_3 torsion, the CH_3 umbrella motion, the CO out-of-plane bending, and the symmetric CC stretching coordinates. The energy of the excited states below 8 eV are essentially invariant to changes in the CH_3 torsion coordinate. The potential energy changes in a similar manner for all PES along the CH_3 umbrella-motion coordinate. Thus, the conclusions regarding the surface crossings do not change. Along the CO out-of-plane bending coordinate, the energy of the 3s Rydberg species increases in the same manner as for the ground-state species. The other Rydberg PESs behave similarly. In contrast, the energy of the $(\pi \rightarrow \pi*)$ species decreases along this coordinate resulting in a crossing between the $(\pi \rightarrow \pi*)$ and the Rydberg surfaces. This feature is identical to what can be deduced from a comparison of Figures 8 and 9, based on results obtained using the sa-CASSCF approach.

The most interesting result relates to the symmetric CC stretching mode because it verifies that the Norrish type-I reaction does not proceed in a concerted manner, at least not at an energy which is easily accessible by photochemistry. Figure 18 shows the schematic reaction coordinate diagram of
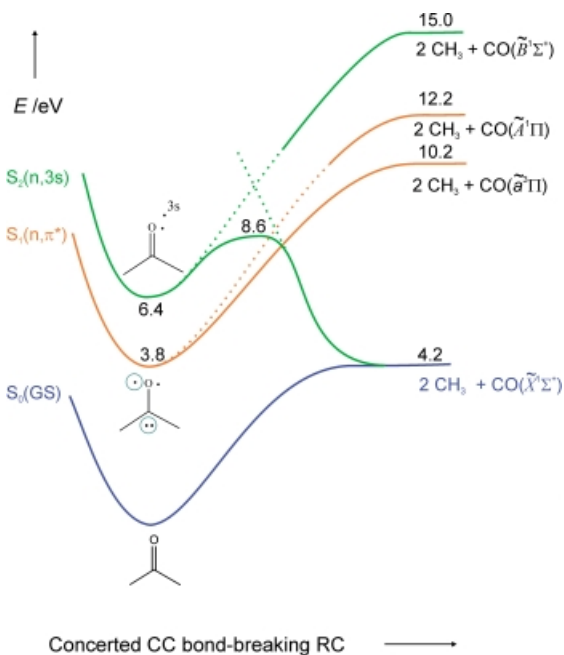

Figure 18. Schematic presentation of the PES along the concerted α-CC bond-breaking reaction coordinate for the S_0(GS), S_1(n,π), and S_2(n,3s) states. Experimental energies [eV] of each excited state and the corresponding product channels are given with respect to the acetone S_0 equilibrium species. The energy barrier for the formation of ground-state products (2 CH_3 + CO) from acetone in the S_2 state is 2.2 eV (TD-B3LYP/6-31 + G(d)).*

acetone on the S_0, S_1, and S_2 PESs along the concerted bond-breaking RC to form the products (2 CH_3 + CO) of different electronic configurations. The S_0 and the S_1 reactions, which have been detailed in papers I and II of this series,[2] give the ground-state and excited-state products, respectively, with the endothermicity between two reactions differing by 6 eV. The energy difference is due to the formation of the first triplet excited state

CO ($\tilde{a}^3\Pi$) from the S_1 PES and the formation of the ground-state CO ($\tilde{X}^1\Sigma^+$) from the S_0 PES. For the S_2 reaction, the second excited-state CO ($\tilde{B}^1\Sigma^+$) should be produced according to the state-correlation principle. This would result in the corresponding product channel to be above the ground-state channel by 10.8 eV. However, the results from the surface-scan calculations indicate that the S_2 PES is connected to the ground-state product channel (CH_3 + CH_3 + CO, all ground-state species), due to an avoided crossing with upper surface of the same symmetry (B_2) via a transition state with an energy barrier of 2.2 eV with respect to the S_2 minimum. Nevertheless, the energy barrier is still much too high to compete with the breakage of a single α-CC bond on the S_2 PES.

2.6. The Acetyl Radical

Because of the significant role of the acetyl radical in the cleavage dynamics of the second α-CC bond of acetone in a stepwise mechanism, we will focus on characterizing the excited-state PESs of the acetyl radical along the CC bond-stretching and the CCO bending coordinates.

2.6.1. Potential Energy Curves Along the CCO Bending Coordinate

Figure 19 shows the ground- and the excited-state potential energy curves of the acetyl radical along the ϕ(CCO) bending coordinate. The geometry was constrained to C_s symmetry throughout the calculations. The geometry at each point was optimized at the B3LYP/6-31 + G(d) level for the ground-state
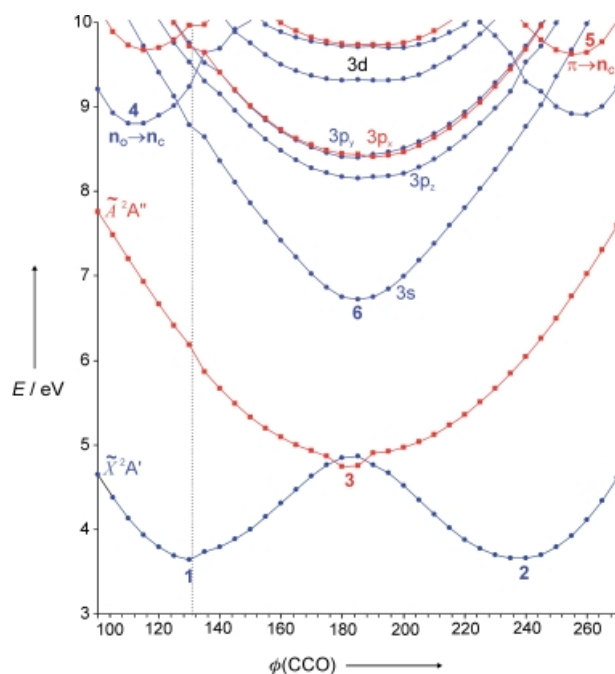

Figure 19. The potential energy curves of the acetyl radical along the ϕ(CCO) bending coordinate calculated at the TD-B3LYP/6-31 + G(d) level under constraint of C_s symmetry. The symmetry of each state is indicated by two colors (A' blue, A'' red). The numbers are those of the structures in Figure 20.

surface ($\tilde{X}^2A'$) and the subsequent single-point excitation-energy calculations were performed at the TD-B3LYP/6-31 + G(d) level of theory. The minima relating to the electronic states of CH$_3$CO$^\bullet$ along the ϕ coordinate also are numbered in Figure 19. These approximate equilibrium geometries were optimized at the B3LYP/6-31 + G(d) level for species **1** – **3**, at the CAS(11,8)/6-31 + G(d) level for species **4** and **5**, and at the CAS(1,7)/6-31 + G(d) level for species **6** and **7**; the results are shown in Figure 20.

The ground state **1** ($\tilde{X}^2A'$, Figure 20) is bent with a calculated ϕ(CCO) bending angle of 128.5°. The SOMO corresponds to a nonbonding orbital located at the central carbon atom (Figure 21). One of the hydrogen atoms of **1** lies in the CCO (y, z)

Figure 20. *The geometries of the stationary points of the acetyl radical calculated at the UB3LYP/6-31 + G(d) level for **1**, **2**, **3**, and the cation, the CAS(11,8)/6-31 + G(d) level for **4** and **5**, and the CAS(1,7)/6-31 + G(d) level for **6** and **7**. The normal-coordinate vectors depicted for **3** and **7** represent the nuclear motions corresponding to the imaginary frequencies of the transition states. The symmetry plane of the species is spanned by H$_1$CCO.*

Figure 21. *The central Kohn – Sham orbitals calculated at the B3LYP/6-31 + G(d) level of theory for A) bent and B) linear acetyl radicals.*

symmetry plane with a H$_1$CCO dihedral angle of 0°. With the CCO angle bent to the other side ($\phi > 180°$), a similar structure of C_s symmetry but with a H$_1$CCO dihedral angle of 180° is given (**2**, $\tilde{X}^2A'$). Species **2** is a transition state in nature, the imaginary frequency corresponds to the CH$_3$ torsional motion that leads to species **1**.

At $\phi = 180°$, the ground state ($\tilde{X}^2A'$) and the first excited state ($\tilde{A}^2A'$) of CH$_3$CO$^\bullet$ are nearly degenerate and the two states will be split along the ϕ(CCO) coordinate; such a splitting is an analogue of the Renner – Teller effect found in the formyl radical (HCO$^\bullet$).[2, 49] However, the SOMO and the LUMO (both are π^*-type orbitals but with different symmetry, Figure 21) are exactly degenerate in linear HCO$^\bullet$ but are slightly different in the case of CH$_3$CO$^\bullet$ due to the influence of the CH$_3$ group in the latter species. The first excited state **3** ($\tilde{A}^2A''$) has been optimized to give a linear CCO configuration as expected. However, the frequency calculation reveals that **3** is actually a transition state. The normal-coordinate vector of the imaginary frequency (1066i cm^{-1}) corresponds to a bending motion orthogonal to the (y, z) symmetry plane. This bending motion will destroy the C_s symmetry and result in a bent C_1 molecule. The minima connected by **3** are two exactly identical ground-state minima (**1**, $\tilde{X}^2A'$) species but with different hydrogen atoms in the symmetry plane.

The second excited state of CH$_3$CO$^\bullet$ corresponds to an excitation from the SOMO to the 3s orbital at larger ϕ(CCO) angles, but it switches to become a valence excited state at small ϕ(CCO) angles. Both species **4** and **5** are valence excited states of CH$_3$CO$^\bullet$ with a bent equilibrium structure, **4** ($^2A'$) corresponds to the excitation primarily from the oxygen nonbonding orbital (SOMO − 1) to the carbon lone-pair orbital (SOMO), **5** ($^2A''$) corresponds to an excitation primarily from the π-orbital (SOMO − 2) to the SOMO. In the structures of species **4** and **5**, the CO bonds are elongated because the π-type orbitals are singly occupied and the CCO bending angles are small, since the SOMO is now doubly occupied. Both valence excited states **4** ($^2A'$) and **5** ($^2A''$) are supposed to cross with the 3s Rydberg state **6** (3s $^2A'$) along the ϕ coordinate, where the crossing may occur at a wider ϕ angle for **4** but it may occur near the minimum of **5** (Figure 19).

In this 3s Rydberg state **6** (Figure 20) both π^* orbitals (Figure 21) are empty and thus no Renner – Teller effect applies, thereby allowing a stable, linear CCO structure. This feature is similar to the cation with a very short CO bond (Figure 20). The 3p Rydberg state also have the lowest energy at ϕ(CCO) = 180°, where the energy of the 3p$_z$ Rydberg state is slightly lower than the 3p$_x$ and 3p$_y$ states (Figure 19).

2.6.2. The CC Bond-Breakage Process

Figure 22 shows various excited-state potential energy curves of the acetyl radical along the CC bond-breaking RC with the CCO
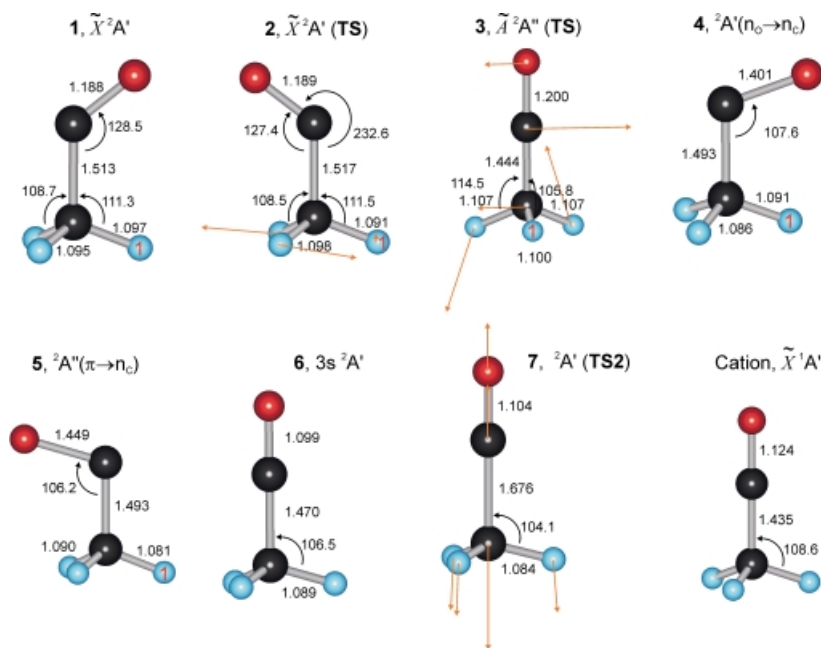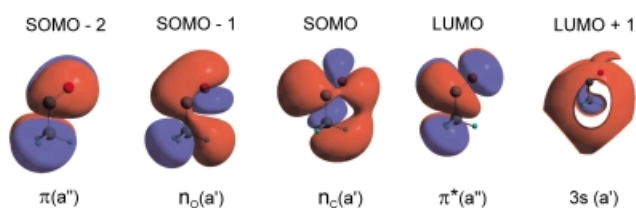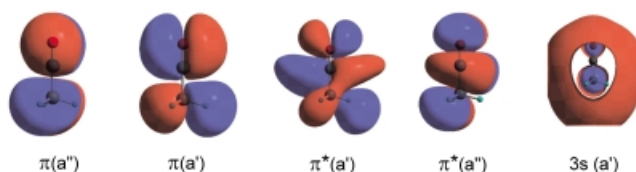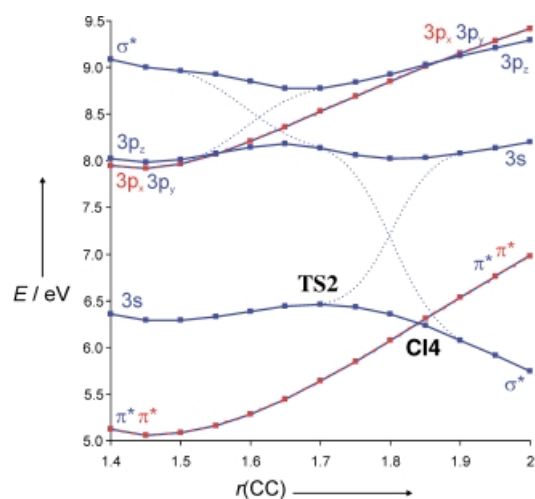
Figure 22. *The potential energy curves of the acetyl radical along the r(CC) bond-breaking coordinate calculated at the state-averaged CAS(1,7)/6-31 + G(d) level of theory with the CCO bending angle constrained to 180°. The symmetry of the states is indicated by two colors (A' blue, A'' red).*

angle, fixed to 180°, imposing C_{3v} geometry. The wavefunction was described by the highest-order Abelian subgroup (C_s). The geometry at each CC distance was optimized at the B3LYP/6-31 + G(d) level on the ground-state cation surface ($\tilde{X}^1A'$) and the subsequent single-point excitation-energy calculations were performed at the CAS(1,7)/6-31 + G(d) level of theory. The active space is described by MOs, which are the $\pi^*(a')/\pi^*(a'')$ pair, the 3s(a'), the $3p_z(a')$, the $3p_y(a')/3p_x(a'')$ pair, and the $\sigma_{cc}^*(a')$ orbitals. As a result, the seven roots of the sa-CASSCF calculations represent the corresponding electronic states of the acetyl radical with the unpaired electron in one of the above mentioned MOs, respectively. These states are indeed described well by the small active space. Including all valence electrons into the active space gives a similar result with the CI coefficient corresponding to the excitation of the $\pi^*(a'')$ of greater than 0.93. Note that the TDDFT calculations at the B3LYP/6-31 + G(d) level of theory give very similar results.

Three points need to be emphasized. First, because ϕ is fixed at 180°, both the first and the second roots ($\tilde{X}^2A'$ and $\tilde{A}^2A''$) are nearly degenerate throughout the calculations along the $r(CC)$ coordinate. Second, the potential curve of the third root corresponds to a pure Rydberg state (3s, $^2A'$) at the minimum region ($r(CC) \sim 1.45$ Å) but relates to a $\sigma_{cc}^*(^2A')$ state at long CC distances ($r(CC) \sim 2.0$ Å). Therefore, a transition state (**TS2**) with a small energy barrier (~ 3 kcal mol^{-1} = 0.03 eV) has been found at $r(CC) \sim 1.7$ Å due to the avoided crossing between the two $^2A'$ surfaces. Note that an avoided crossing between the $3p_z$ and the σ_{cc}^* states also appears at an intermediate CC distance ($r(CC) \sim 1.65$ Å). Third, along the $r(CC)$ coordinate the $3s/\sigma_{cc}^*$ potential curve goes down, after passing over **TS2**, to give the ground-state products $CH_3(\tilde{X}^2A_2'') + CO(\tilde{X}^1\Sigma^+)$, whereas the coupled $\pi^*(^2A')/\pi^*(^2A'')$ potential curves persist to increase in energy to give the excited-state products $CH_3(\tilde{X}^2A_2'') + CO(\tilde{A}^3\Pi)$. As a consequence, a curve crossing is shown in Figure 22 at $r(CC) \sim 1.9$ Å and a conical intersection is anticipated in that region.

The feature of the conical intersection can be very well viewed from a 2D PES shown in Figure 23, where the characteristic double-cone topology is demonstrated by the two intersecting A' surfaces, whereas the A'' surface does not couple with the A'' states. After internal conversion to the lower surface, the molecule can either directly break the CC bond to form the ground-state products or go back to the $^2A'/^2A''$ states first and then break the CC bond from the hot (bent) ground state.
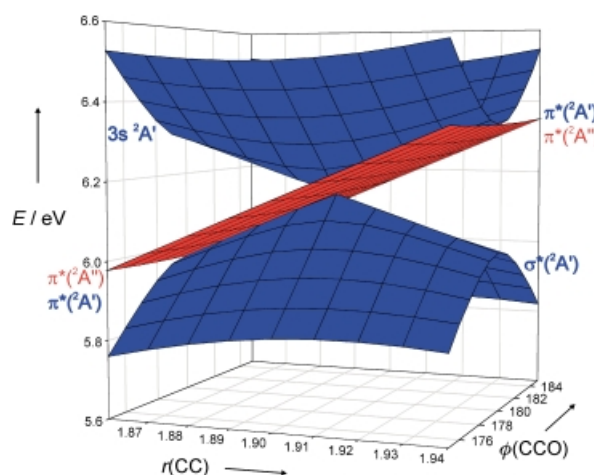

Figure 23. *The three lowest doublet PESs of the acetyl radical calculated at the state-averaged CAS(1,7)/6-31 + G(d) level of theory along the r(CC) stretching and the ϕ(CCO) bending coordinates in the region around **CI4**.*

2.7. A General Overview of Norrish Type-I Reactions

We have shown in paper I of this series that ground-state acetone forms ground-state acetyl and methyl radicals, and that this path is lowest in energy. In numerous thermal experiments, the products are usually CH_4 and CH_2CO but this channel is the result of bimolecular reactions and not unimolecular thermal decompositions. Our results are entirely consistent with recent infrared multiphoton dissociation investigations of ground-state gaseous acetone molecules[50] as discussed in the next paper.[45] For the excited state, the involvement of the nonbonding electron on oxygen is crucial in defining the active space.

The theoretical results are summarized in Figure 24 for the stepwise α-cleavage reaction on the two lower-lying excited singlet surfaces (S$_2$(n,3s) and the S$_1$(n$_y$,π^*) PESs). A subset of the involved species and the corresponding electronic configurations are also shown. The common feature of the α-cleavage on both the S$_2$ and the S$_1$ PESs is the formation of the ground-state products (2 CH$_3$ + CO) via a linear acetyl species. However, the fate of the linear acetyl species is different in the two cases. For the S$_2$ state (green curve), the linear 3s acetyl reaches a **CI** through a first-order saddle point (**TS2**) that gives rise to a small barrier; in the **CI** the 3s $^2A'$, $\tilde{A}^2A''$, and $\tilde{X}^2A'$ states are degenerate. Branching at the **CI** results in either direct bond cleavage or internal conversion to the $\tilde{A}^2A''/\tilde{X}^2A'$ surfaces and subsequent bond breakage on the ground-state surface. On the S$_1$ PES (orange curve), the initially bent structure following the barrier crossing (~ 0.8 eV relative to S$_1$) moves towards the linear
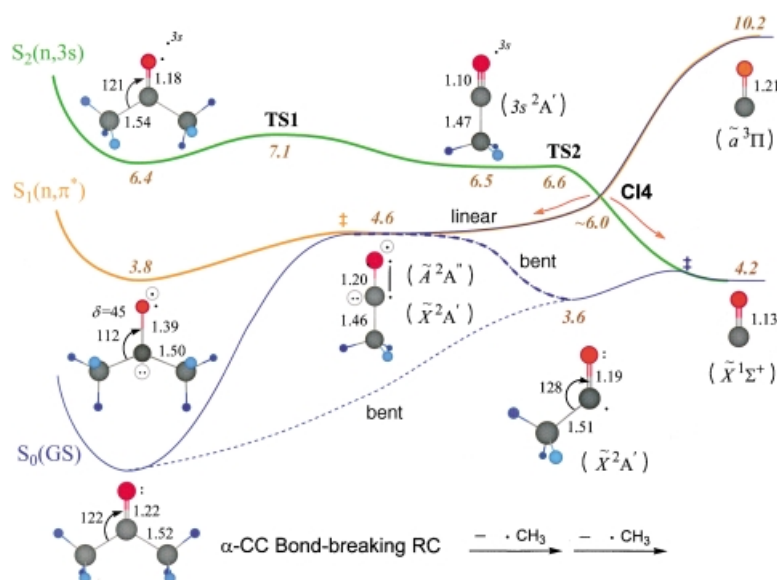
Figure 24. *Schematic PES along the first and the second α-CC bond-breaking reaction coordinate for the S_0(GS), S_1(n,π*), and S_2(n,3s) states. Both nuclear and electronic structures of the central stationary points are shown and the corresponding energies [eV] relative to the acetone S_0 minimum are given.*

geometry of the acetyl radical. The linear acetyl species ($\tilde{A}^2A''$) then internally converts (with near degeneracy of the surfaces) to form a ground-state species ($\tilde{X}^2A'$) through the CCO bending motion (the corresponding path represented by the dotted blue curve); the CC bond breakage occurs on the ground-state surface ($\tilde{X}^2A'$). Note that the thermal CC bond-breakage process of acetone occurring on the S_0 PES is different (not shown) in the manner that it does not involve a linear acetyl species.[2]

The α-cleavage of the first bond of acetone on the S_2 PES involves a transition state (**TS1**) and an energy barrier of ~ 0.7 eV. The barrier is induced by the formation of a CO π-bond when the first α-CC σ-bond breaks. This feature is similar to what we have found on the S_1 PES.[2] Therefore, the CCO bending angle will in both cases approach 180°. The CO bond on the S_2 PES is much shorter than on the S_1 PES, and the (y, z) molecular symmetry plane is maintained ($\delta = 0$) on the S_2 PES but broken ($\delta \neq 0$) through the CO out-of-plane bending motion on the S_1 PES. These differences arise from the different electronic configurations in the two cases, namely from the fact that the unpaired electron resides in the 3s and in the π* orbitals, respectively.

The above α-cleavage mechanism of acetone in the 3s state can be considered a general case to represent higher-lying Rydberg states. The fundamental aspect is the unpaired electron in the n_y orbital of the oxygen atom after excitation; the possibility exists to form a new π-bond through overlap between this electron and the electron that becomes available when the CC σ-bond is broken. This mechanism does not apply for the ($\pi \rightarrow \pi$*) and the ($n_z \rightarrow \pi$*) excited states, where in both cases the n_y orbital is doubly occupied. This double occupancy prevents the formation of a new π-bond and results in a much higher energy barrier upon breakage of the α-CC bond. This

scenario resembles the decomposition on the ground-state surface. The variation in the energy barrier for α-cleavage from different electronic states of acetone is illustrated in Scheme 1.

3. Concluding Remarks

We have employed various levels of CASSCF and TDDFT calculations to provide an internally consistent picture of reactions from the highly excited electronic states of acetone with a focus on the states that are involved in the photochemical and photophysical processes at excitation energies around 8 eV. The goal is to unify the wide variety of experimental results for the dynamics of the Norrish type-I reaction that have been reported previously. We have characterized an efficient pathway for internal conversion that, via the CO stretching mode and two conical intersections (**CI2** and **CI3**), connects the highly excited Rydberg states with the S_2 state. The key mediators of the process are the ($\pi \rightarrow \pi$*) and the ($n_z \rightarrow \pi$*) surfaces. Because of the significantly different electronic characteristics of the valence and Rydberg excited states, the topology
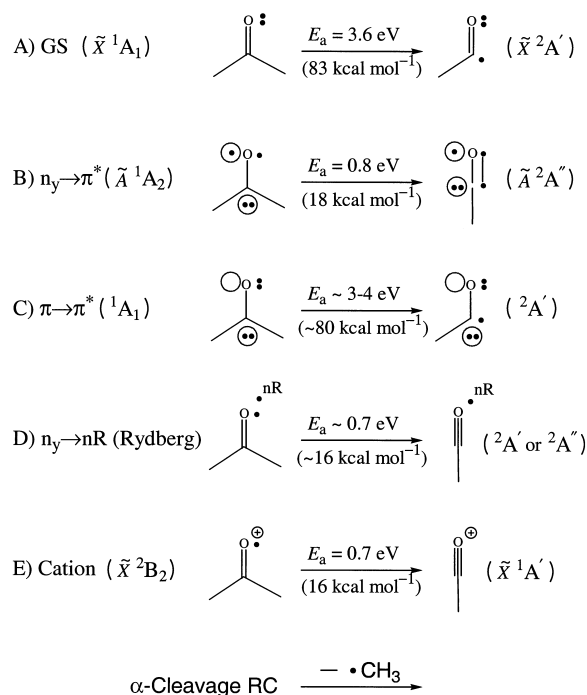
Scheme 1. *Decomposition of acetone from various excited states. E_a represents the energy barrier above the ZPE of the corresponding state.*

along the CO stretching coordinate is very different in the two cases and crossings result. The S_1 state can be reached from the S_2 state through a sloped **CI** (**CI1**). The passing of such a sloped **CI** more closely resembles a process with an energy barrier. It is therefore not as efficient as in the case of funneling through a conventional **CI** (such as **CI2**). In the specific case of **CI1**, the

barrier height is substantial especially when the CO out-of-plane bending motion is taken into account. The most energetically favorable reaction pathway on the S_2 surface is the *stepwise* α-cleavage process. The energy barrier along the single α-CC bond-breaking RC on the S_2 PES is lower than the energy of **CI1** that connects the S_1 and S_2 surfaces. This shows that Norrish type-I reactions can occur on the S_2 surface, particularly when the molecule lands on S_2 from a higher-lying state and therefore possesses the needed internal energy to surmount the barrier.

From a dynamic point of view, two different reaction paths on the S_2 PES can be followed after passing of **CI2**. On one hand, if the gradient difference vector (x_1) is followed, the corresponding CO stretching motion would lead to either the ($\pi \rightarrow \pi^*$) species (at long CO distances) or the ($n_y \rightarrow 3s$) species (at short CO distances). On the other hand, if the nonadiabatic coupling vector (x_2) is followed, the corresponding asymmetric CC stretching motion would immediately give rise to α-bond cleavage and produce a 3s linear acetyl radical. The branching of the reaction paths is determined by the symmetry of the activated vibrational motions upon excitation. For example, if the a_1 CO stretching motion is activated upon one-photon excitation, it would lead to a ($\pi \rightarrow \pi^*$) species; if the b_2 asymmetric CC stretching is activated upon two-photon excitation, it will give the α-cleavage products. It is particularly worth noticing that the involvement of the "bound" ($\pi \rightarrow \pi^*$) state can rationalize differences between two-photon and one-photon experiments involving acetone (and other ketones) excited to ~ 8 eV; the details will be discussed in our accompanying paper that describes the experimental aspects for acetone and other acyclic as well as cyclic ketones.[45]

[1] W. A. Noyes, Jr. in *Photochemistry and Reaction Kinetics* (Eds.: P. G. Ashmore, F. S. Dainton, T. M. Sugden), Cambridge University Press, Cambridge, **1967**, pp. 1 – 25.

[2] a) E. W.-G. Diau, C. Kötting, A. H. Zewail, *ChemPhysChem* **2001**, *2*, 273 – 293; b) E. W.-G. Diau, C. Kötting, A. H. Zewail, *ChemPhysChem* **2001**, *2*, 294 – 309.

[3] a) S. K. Kim, S. Pedersen, A. H. Zewail, *J. Chem. Phys.* **1995**, *103*, 477 – 480; b) S. K. Kim, A. H. Zewail, *Chem. Phys. Lett.* **1996**, *250*, 279 – 286; c) S. K. Kim, J. Guo, J. S. Baskin, A. H. Zewail, *J. Phys. Chem.* **1988**, *100*, 9202 – 9205.

[4] a) S. Pedersen, J. L. Herek, A. H. Zewail, *Science* **1994**, *266*, 1359 – 1364; b) E. W.-G. Diau, J. L. Herek, Z. H. Kim, A. H. Zewail, *Science* **1998**, *279*, 847 – 851.

[5] D. A. Hansen, E. K. C. Lee, *J. Chem. Phys.* **1975**, *62*, 183 – 189.

[6] Y. Haas, *Spectrochim. Acta Part A* **1990**, *46*, 541 – 549, and references therein.

[7] E. K. C. Lee, *Acc. Chem. Res.* **1977**, *10*, 319 – 326, and references therein.

[8] a) G. A. Gaines, D. J. Donaldson, S. J. Strickler, V. Vaida, *J. Phys. Chem.* **1988**, *92*, 2762 – 2766; b) D. J. Donaldson, G. A. Gaines, V. Vaida, *J. Phys. Chem.* **1988**, *92*, 2766 – 2769.

[9] R. McDiarmid, *J. Chem. Phys.* **1991**, *95*, 1530 – 1536.

[10] J. G. Philis, L. Goodman, *J. Chem. Phys.* **1993**, *98*, 3795 – 3802.

[11] a) P. Brint, L. O'Toole, S. Couris, D. Jardine, *J. Chem. Soc. Faraday Trans.* **1991**, *87*, 2891 – 2895; b) L. O'Toole, P. Brint, C. Kosmidis, G. Boulakis, P. Tsekeris, *J. Chem. Soc. Faraday Trans.* **1991**, *87*, 3343 – 3351.

[12] a) D. J. Donaldson, S. R. Leone, *J. Chem. Phys.* **1986**, *85*, 817 – 824; b) E. L. Woodbridge, T. R. Fletcher, S. R. Leone, *J. Phys. Chem.* **1988**, *92*, 5387 – 5393.

[13] P. D. Lightfoot, S. P. Kirwan, M. J. Pilling, *J. Phys. Chem.* **1988**, *92*, 4938 – 4946.

[14] K. A. Trentelman, S. H. Kable, D. B. Moss, P. L. Houston, *J. Chem. Phys.* **1989**, *91*, 7498 – 7513.

[15] G. E. Hall, V. Bout, T. J. Sears, *J. Chem. Phys.* **1991**, *94*, 4182 – 4188.

[16] S. W. North, D. A. Blank, J. D. Gezelter, C. A. Longfellow, Y. T. Lee, *J. Chem. Phys.* **1995**, *102*, 4447 – 4460.

[17] Q. Zhong, L. Poth, A. W. Castleman, Jr., *J. Chem. Phys.* **1999**, *110*, 192 – 196.

[18] a) J. C. Owrutsky, A. P. Baronavski, *J. Chem. Phys.* **1998**, *108*, 6652 – 6659; b) J. C. Owrutsky, A. P. Baronavski, *J. Chem. Phys.* **1999**, *110*, 11 206 – 11 213; c) A. P. Baronavski, J. C. Owrutsky, *Chem. Phys. Lett.* **2000**, *333*, 36 – 40.

[19] a) R. McDiarmid, A. Sabljić, *J. Chem. Phys.* **1988**, *89*, 6086 – 6095; b) J. G. Philis, J. M. Berman, L. Goodman, *Chem. Phys. Lett.* **1990**, *167*, 16 – 20; c) T. Kundu, S. N. Thakur, L. Goodman, *J. Chem. Phys.* **1992**, *97*, 5410 – 5416; d) X. Xing, R. McDiarmid, J. G. Philis, L. Goodman, *J. Chem. Phys.* **1993**, *99*, 7565 – 7573; e) R. T. Wiedmann, L. Goodman, M. G. White, *Chem. Phys. Lett.* **1998**, *293*, 391 – 396; f) D. A. Shea, L. Goodman, M. G. White, *J. Chem. Phys.* **2000**, *112*, 2762 – 2767.

[20] Y. F. Zhu, S. L. Allman, R. C. Phillips, W. R. Garrett, C. H. Chen, *Chem. Phys.* **1996**, *202*, 175 – 184.

[21] S. N. Thakur, D. Guo, T. Kundu, L. Goodman, *Chem. Phys. Lett.* **1992**, *199*, 335 – 340.

[22] R. McDiarmid, X. Xing, *J. Chem. Phys.* **1997**, *107*, 675 – 679.

[23] M. R. J. Hachey, F. Grein in *The Role of Rydberg States in Spectroscopy and Photochemistry* (Ed.: C. Sandorfy), Kluwer Academic, Dordrecht, **1999**, pp. 179 – 230.

[24] B. Hess, P. J. Bruna, R. J. Buenker, S. D. Peyerimhoff, *Chem. Phys.* **1976**, *18*, 267 – 280.

[25] V. Galasso, *J. Chem. Phys.* **1990**, *92*, 2495 – 2504.

[26] S. R. Gwaltney, R. J. Bartlett, *Chem. Phys. Lett.* **1995**, *241*, 26 – 32.

[27] D. W. Liao, A. M. Mebel, M. Hayashi, Y. J. Shiu, Y. T. Chen, S. H. Lin, *J. Chem. Phys.* **1999**, *111*, 205 – 215.

[28] M. Merchán, B. O. Roos, R. McDiardmid, X. Xing, *J. Chem. Phys.* **1996**, *104*, 1791 – 1804.

[29] P. Farmanara, V. Stert, W. Radloff, *Chem. Phys. Lett.* **2000**, *320*, 697 – 702.

[30] K. B. Wiberg, R. E. Stratmann, M. J. Frisch, *Chem. Phys. Lett.* **1998**, *297*, 60 – 64.

[31] D. J. Tozer, N. C. Handy, *Phys. Chem. Chem. Phys.* **2000**, *2*, 2117 – 2121.

[32] A CAS(8,17) calculation would be required to describe all the states in Table 1. Such a calculation cannot be handled by the MOLPRO program package.[51] Therefore, the tabulated results (Table 1) were obtained from a CAS(8,16) calculation less the $3d_{xz}(b_1)$ orbital. The excitation energy for the $A_2(n_y \rightarrow 3d_{xz})$ Rydberg state was obtained based on a similar sa-CASSCF calculation with the $3d_{xz}(b_1)$ orbital in the active space but with either the $p_x(b_1)$ or the $p_y(b_2)$ orbitals out of the active space.

[33] F. Jensen, *Introduction to Computational Quantum Chemistry*, Wiley, New York, NY, **1999**.

[34] J. J. W. McDouall, K. Peasley, M. A. Robb, *Chem. Phys. Lett.* **1988**, *148*, 183 – 189.

[35] K. Andersson, P. Malmqvist, B. O. Roos, *J. Chem. Phys.* **1992**, *96*, 1218 – 1226.

[36] M. Klessinger, J. Michl, *Excited States and Photochemistry of Organic Molecules*, VCH, New York, NY, **1995**.

[37] M. A. Robb, M. Garavelli, M. Olivucci, F. Bernard in *Reviews in Computational Chemistry, Vol. 15* (Eds.: K. B. Lipkowitz, D. B. Boyd), Wiley-VCH, New York, NY, **2000**, pp. 87 – 146, and references therein.

[38] I. N. Ragazos, M. A. Robb, F. Bernardi, M. Olivucci, *Chem. Phys. Lett.* **1992**, *197*, 217 – 223.

[39] W. Domcke, G. Stock, *Adv. Chem. Phys.* **1997**, *100*, 1 – 169.

[40] D. R. Yarkony, *Acc. Chem. Res.* **1998**, *31*, 511 – 518.

[41] M. Klessinger, *Angew. Chem.* **1995**, *107*, 597 – 599; *Angew. Chem. Int. Ed. Engl.* **1995**, *34*, 549 – 551.

[42] F. Bernardi, M. Olivucci, M. A. Robb, *Chem. Soc. Rev.* **1996**, *25*, 321 – 328.

[43] S. Wilsey, K. N. Houk, A. H. Zewail, *J. Am. Chem. Soc.* **1999**, *121*, 5772 – 5786, and references therein.

[44] a) E. W.-G. Diau, O. K. Abou-Zied, A. A. Scala, A. H. Zewail, *J. Am. Chem. Soc.* **1998**, *120*, 3245 – 3246; b) D. Zhong, E. W.-G. Diau, T. M. Bernhardt, S. De Feyter, J. D. Roberts, A. H. Zewail, *Chem. Phys. Lett.* **1998**, *298*, 129 – 140; c) E. W.-G. Diau, S. De Feyter, A. H. Zewail, *Chem. Phys. Lett.* **1999**, *304*, 134 – 144; d) E. W.-G. Diau, S. De Feyter, A. H. Zewail, *J. Chem. Phys.* **1999**, *110*, 9785 – 9788; e) S. De Feyter, E. W.-G. Diau, A. H. Zewail, *Phys. Chem. Chem. Phys.* **2000**, *2*, 877 – 883.

[45] T. I. Sølling, E. W.-G. Diau, C. Kötting, S. De Feyter, A. H. Zewail, *Chem-PhysChem* **2002**, *3*, 79 – 97, immediately following this paper.

[46] *Gaussian 98 (Revision A.9)*, M. J. Frisch, G. W. Trucks, H. B. Schlegel, G. E. Scuseria, M. A. Robb, J. R. Cheeseman, V. G. Zakrzewski, J. A. Montgomery, R. E. Stratmann, J. C. Burant, S. Dapprich, J. M. Millam, A. D. Daniels, K. N. Kudin, M. C. Strain, O. Farkas, J. Tomasi, V. Barone, M. Cossi, R. Cammi, B. Mennucci, C. Pomelli, C. Adamo, S. Clifford, J. Ochterski, G. A. Petersson, P. Y. Ayala, Q. Cui, K. Morokuma, D. K. Malick, A. D. Rabuck, K. Raghava-chari, J. B. Foresman, J. Cioslowski, J. V. Ortiz, B. B. Stefanov, G. Liu, A. Liashenko, P. Piskorz, I. Komaromi, R. Gomperts, R. L. Martin, D. J. Fox, T. Keith, M. A. Al-Laham, C. Y. Peng, A. Nanayakkara, C. Gonzalez, M. Challacombe, P. M. W. Gill, B. G. Johnson, W. Chen, M. W. Wong, J. L. Andres, M. Head-Gordon, E. S. Replogle, J. A. Pople, Gaussian, Inc., Pittsburgh, PA, **1998**.

[47] For example, in an initial CAS(8,7) full optimization process starting from a geometry with the in-plane CH bond length of 1.09 Å, the energies of the third and the fourth roots were calculated to be -191.78680 and -191.76474 hartree, respectively, with the energy gap between the two roots being 0.60 eV. However, during the optimization the two CH bond distances were continuously increased and the total energy of the fourth root reached -191.63091 hartree whereas the energy gap between the two states corresponding the third and the fourth root decreased to 0.04 eV at a CH bond length of 1.44 Å.

[48] Notice that the frequency calculation gives three imaginary frequencies: 865i (a′), 96i (a′′), and 89i cm^{-1} (a′). However, the latter two motions do not affect the IRC analysis because the Gaussian 98[46] IRC program defaults to follow the largest of the imaginary modes.

[49] A. Loettgers, A. Untch, H. Keller, R. Schinke, H. Werner, C. Bauer, P. Rosmus, *J. Chem. Phys.* **1997**, *106*, 3186 – 3204, and references therein.

[50] C. L. Berrie, C. A. Longfellow, A. G. Suits, Y. T. Lee, *J. Phys. Chem. A* **2001**, *105*, 2557 – 2562.

[51] H.-J. Werner, P. J. Knowles, *MOLPRO*, University of Birmingham, Birming-ham, **2000**; http://www.tc.bham.ac.uk/molpro/.